On the Momentum Flux of Internal Tides

CALLUM J. SHAKESPEARE

Research School of Earth Sciences, Australian National University, Canberra, Australia

ANDREW MCC. HOGG

*Research School of Earth Sciences, and ARC Centre of Excellence in Climate Extremes,
Australian National University, Canberra, Australia*

ABSTRACT

The action of the barotropic tide over seafloor topography is the major source of internal waves at the bottom of the ocean. This internal tide has long been recognized to play an important role in ocean mixing. Here it is shown that the internal tide is also associated with a net (domain integrated) momentum flux. The net flux occurs as a result of the Doppler shifting of the internal tide at the point of generation by near-bottom mean flows. Linear theory is presented that predicts the amplitude of the wave momentum flux. The net flux scales with the bottom flow speed and the topographic wavenumber to the fourth power and is directed opposite to the bottom flow. For realistic topography, the predicted peak momentum flux occurs at scales of order 10 km and smaller, with magnitudes of order 10^{-3}–$10^{-2}\,\mathrm{N\,m^{-2}}$. The theory is verified by comparison with a suite of idealized internal wave-resolving simulations. The simulations show that, for the topography considered, the wave momentum flux radiates away from the bottom and enhances mean and eddying flow when the tidal waves dissipate in the upper ocean. Our results suggest that internal tides may play an important role in forcing the upper ocean.

1. Introduction

Internal tides, or tidally generated internal waves, are a ubiquitous feature of the World Ocean, generated when the large-scale barotropic tide flows over rough seafloor topography. The internal waves are generated at the tidal frequency, or its harmonics (Bell 1975a), and their horizontal wavelength is determined by the scale of the local topography. The structure and behavior of these waves depends on whether their vertical wavelength is small or large compared with the ocean depth. Larger-scale topography (~100 km) generates waves with larger vertical wavelengths that feel the effect of the ocean surface and form low-mode internal tides that, as the name suggests, are well described in terms of a modal decomposition. These low-mode tides propagate large horizontal distances and tend to dissipate their energy remotely—for example, on continental shelves (Nash et al. 2004)—or interact further with topography, scattering, or radiating smaller-scale waves

(e.g., St. Laurent and Garrett 2002). Smaller-scale topography (~10 km or smaller) generates tidal waves with vertical wavelengths significantly smaller than the ocean depth. These small-scale internal tides form distinct, vertically propagating tidal beams and are more likely to dissipate and otherwise interact with the local flow. The energy flux associated with these waves, and their breaking and dissipation in the deep ocean, is thought to be important in maintaining the abyssal circulation of the ocean (St. Laurent and Garrett 2002; Kunze 2017). However, not all the small-scale internal tide dissipates in the deep ocean and little attention has been given to the waves that escape this region and propagate into the upper ocean. Waves which span the ocean depth are potentially important, since small-scale internal tides are also associated with vertical fluxes of momentum that can act to accelerate the local flow when the waves dissipate, thereby driving the upper ocean.

The momentum transport by internal waves and the phenomenon of internal wave-driven flow has not been a focus of oceanographic research but has a long history in the atmospheric literature (e.g., White 1949).

Corresponding author: Callum J. Shakespeare, callum.shakespeare@anu.edu.au

The waves in question are topographic lee waves, but the principle can be generalized to all internal waves. The seminal work of Eliassen and Palm (1961) showed that waves carry both energy and momentum as they propagate vertically. The momentum is extracted from the solid earth through topographic form stress when the waves are generated. This "wave momentum flux" (or more correctly, the pseudomomentum flux; see McIntyre 1981) is conserved as the waves propagate in a uniform medium. Booker and Bretherton (1967) showed that, in a vertically sheared flow, the waves will approach a singularity at "critical levels" where their phase speed goes to zero and the waves dissipate and deposit their momentum. More generally, where background rotation is important, the same process occurs at "inertial levels" where the Doppler (down)shifted wave frequency matches the local Coriolis frequency (e.g., Xie and Vanneste 2017).[1] Thus, internal waves provide a mechanism to force circulation at height above their site of generation and, in the absence of reflections, *must* do so to conserve momentum. These concepts of wave forcing were formalized by Andrews and McIntyre (1976) into the "non-acceleration theorem," which states that internal waves conserve their directionally and temporally averaged (generalized) momentum flux in the absence of dissipative processes; the generalized momentum flux is called the Eliassen–Palm (EP) flux and is a combination of the vertical flux of horizontal momentum and horizontal buoyancy flux. The divergence of the EP flux has since been widely used to evaluate the wave forcing of the atmospheric circulation (e.g., Miyahara et al. 1993). The importance of wave momentum fluxes in forcing the stratospheric circulation is now well recognized, and parameterized wave drag forms an important part of weather and climate modeling (e.g., McFarlane 1987; Bühler 2014).

In the oceanographic literature, the EP flux and nonacceleration theorem have appeared only sparingly. McPhaden et al. (1986) used these theoretical tools to investigate the interaction of equatorial Kelvin waves with zonal jets. Eden and Olbers (2017) used an equivalent residual-mean theory to formulate a closure for internal wave–mean flow interactions. More commonly, the EP formalism has been employed in the context of diagnosing eddy fluxes (e.g., Maddison and Marshall 2013).

Oceanic internal waves have long been recognized as important in providing energy for deep-ocean mixing (Munk 1981) and past studies have focused on energy flux radiated from topography, with little consideration of the momentum flux. Recently, the momentum flux has been considered to a limited extent in the context of lee waves. Lee waves are associated with a momentum flux opposite to the direction of the flow responsible for their generation (e.g., Bell 1975b). If the lee waves dissipate local to their generation site, they act as a drag on the flow. Building off the pioneering work of Bell (1975b), Naveira Garabato et al. (2013) computed the lee wave momentum flux using topographic survey data and climatology for the global ocean. Their results suggest that the acceleration (or deceleration) of the flow due to the dissipation of lee waves plays a significant role in the dynamics of the Southern Ocean. Trossman et al. (2016) parameterized the lee wave momentum flux in an eddying global model, assuming that the waves dissipate in the bottom 500 m, thereby applying a local drag on the flow. This lee wave drag drives substantial changes in the distribution of ocean kinetic energy in their simulations. A further example of internal wave momentum fluxes in the oceanographic literature is Muench and Kunze (2000), who showed that forcing by internal waves provides one mechanism to enhance and sustain the Pacific equatorial deep jets.

The forcing of mean flow by the radiating internal tide specifically—as opposed to other waves—has seen even less discussion in the literature. Grisouard and Bühler (2012) examined the generation of mean flow due to the direct damping of tidal waves by a Rayleigh drag in an idealized setting. As with the lee wave problem, the effective force on the mean flow is felt in locations of wave dissipation which may be distant from the generation site. Pinkel et al. (2012) measured internal tide EP fluxes at the Kaena Ridge near Hawaii and proposed that they may play a role in driving upper ocean mean flow.

Here we directly compute the momentum flux of the internal tide and investigate the mean flow response. We show that the generation of the internal tide produces a *net* (time and space averaged) momentum flux in the presence of a steady near-bottom flow. This result follows from Bell (1975b) but was not discussed therein. The presence of the bottom flow acts to Doppler shift the generated waves and thereby biases the momentum (and energy) fluxes into the upstream tidal waves. This behavior is contrary to the usual picture of barotropic tidal generation where waves are generated in a symmetric fashion with two equal and opposite tidal beams. A similar problem has recently been examined by Lamb and Dunphy (2018). They develop an idealized two-dimensional model (without rotation) to show that the Doppler shift associated with a surface-trapped steady current causes asymmetry in the horizontal

---

[1] The terms "inertial level" and "critical level" are often used interchangeably (e.g., Kunze 1985).

energy fluxes. Here we look at the impact of bottom flows on the momentum fluxes in a more realistic setting. As noted by Lamb and Dunphy (2018), "the effects of a mean flow ... on internal wave generation by tide–topography interactions have not been previously considered in numerical or theoretical studies."

One of the major complications in analyzing the impact of internal waves in a numerical model is distinguishing the waves from the nonwave flow (which includes both the time-mean and eddying flow). Here we perform this separation using the Lagrangian filtering methodology of Shakespeare and Hogg (2018, 2017a), which defines waves as motions that have a frequency moving with the flow (a Lagrangian frequency) exceeding the inertial frequency, consistent with the hydrostatic internal wave dispersion relation. This filtering results in a well-defined wave field and the ability to rigorously evaluate wave quantities such as the momentum flux. A well-defined wave field also implies a well-defined nonwave (total minus wave) flow and thus allows quantification of the nonwave flow response to wave forcing, even when the wave field is of a similar order.

The paper is set out as follows. In section 2 we employ linear theory to derive an expression for the net momentum flux of the internal tide. In section 3 we introduce a numerical model to verify this theory. In section 3b we show that the impact of the wave momentum flux is to drive mean flow and enhance eddying flow in the upper ocean. In section 4 we compare the flow regime of the global ocean to that of our idealized model. In section 5 we conclude.

2. Theory

Here we derive the expression for the momentum flux associated with the internal tide. The key result to be shown is that in the absence of a mean bottom flow, momentum is equally and oppositely distributed into the wave field, with zero net momentum extraction. However, when a mean bottom flow is present, net momentum is extracted from the solid earth at generation. In either case, the momentum is transferred to the mean flow where the waves break or otherwise dissipate, but can only drive a domain-averaged mean flow in the latter case.

a. The Eliassen–Palm flux and wave-forced equations

The horizontal momentum equation for an (inviscid) rotating fluid may be written as

$$\left(\frac{\partial}{\partial t} + \mathbf{u} \cdot \nabla\right)\mathbf{u}_h + f\hat{\mathbf{z}} \times \mathbf{u}_h = -\nabla_h p, \qquad (1)$$

where (u, v, w) are the velocities in the (x, y, z) Cartesian coordinate directions, p the dynamic pressure, and f the Coriolis frequency. The subscript h denotes the horizontal component of the vector. Each field (e.g., p) may be divided into a wave component $\tilde{p}$ and a nonwave (mean and eddy) $\overline{p}$ component; that is, $p = \tilde{p} + \overline{p}$. We assume that the product of an appropriately separated wave and nonwave field is zero in a time–horizontal-space (xyt) average, denoted by angled brackets; for example, $\langle \tilde{p}\overline{p}\rangle \equiv 0$. With this assumption, the time–space-averaged momentum equation (1) may be written as

$$\frac{\partial\langle\overline{\mathbf{u}}_h\rangle}{\partial t} + \frac{\partial}{\partial z}\langle\overline{\mathbf{u}}_h\overline{w}\rangle + f\hat{\mathbf{z}} \times \langle\overline{\mathbf{u}}_h^*\rangle = -\frac{\partial\langle\mathbf{F}_{\text{EP}}\rangle}{\partial z} - \langle\nabla_h\overline{p}\rangle, \qquad (2)$$

where $\mathbf{F}_{\text{EP}}$ is the EP flux (Andrews and McIntyre 1976; Xie and Vanneste 2017) defined by

$$\mathbf{F}_{\text{EP}} = \left(\tilde{u}\tilde{w} - \frac{f\tilde{v}\tilde{b}}{N^2}, \tilde{v}\tilde{w} + \frac{f\tilde{u}\tilde{b}}{N^2}, 0\right) = \tilde{\mathbf{u}}_h\tilde{w} + f\hat{\mathbf{z}} \times \frac{\tilde{\mathbf{u}}_h\tilde{b}}{N^2}, \qquad (3)$$

for mean stratification $\langle\partial_z b\rangle \equiv N^2$, and the *residual velocity* is

$$\overline{\mathbf{u}}_h^* = \overline{\mathbf{u}}_h - \frac{\partial}{\partial z}\frac{\langle\tilde{\mathbf{u}}_h\tilde{b}\rangle}{N^2}. \qquad (4)$$

Terms involving horizontal derivatives of velocity do not appear in the domain-averaged momentum budget (2) owing to the xy averaging. The terms in (2) are, from left to right, the acceleration of the nonwave (mean) flow, divergence of the nonwave momentum flux, Coriolis, divergence of the EP flux, and pressure differences across rough topography and/or between domain edges. Since our nonwave field includes both mean flow and eddies, the nonwave momentum flux $\langle\overline{\mathbf{u}}_h\overline{w}\rangle$ is likely to be predominately associated with eddying flow.

Observant readers will note that a wave buoyancy flux $\langle\tilde{\mathbf{u}}_h\tilde{b}\rangle$ has been added to both sides of (2) to yield the form shown. The reason for this addition is to obtain the EP flux divergence as the wave forcing term on the right-hand side since it is the EP flux—and not the wave momentum flux, $\langle\tilde{\mathbf{u}}_h\tilde{w}\rangle$—that is equal to the force exerted on the topography during internal tide generation (Bell 1975b). The radiating EP flux is conserved for small-amplitude waves in a slowly varying mean flow in the absence of dissipation (Bretherton 1969; Bell 1975b). Therefore, the presence of vertical divergences in the horizontally averaged EP flux $\langle\partial_z\mathbf{F}_{\text{EP}}\rangle$ indicates where the waves are dissipating, depositing momentum, and thereby accelerating the nonwave flow. The same cannot be said for the wave momentum

flux $\langle \tilde{\mathbf{u}}_h \tilde{w} \rangle$, which is *not* conserved, even in the absence of dissipation.

b. The EP flux of the internal tide

In the "usual" linear theory, the generation of internal tides produces zero net EP flux since momentum is equally and oppositely distributed into two tidal beams in the absence of any mean flow (even for anisotropic topography, as shown below). Here we consider a background state with uniform horizontal flow $\mathbf{U}_0 = (U_0, V_0, 0)$, in addition to a tidal flow assumed (without loss of generality) to be oriented in the x direction $U_t \cos(\omega_t t)\hat{\mathbf{x}}$. We demonstrate that this configuration leads to a net EP flux. This result is consistent with prior work by Bell (1975b), who obtains a similar result for the wave EP flux (wave stress) for a system with mean and tidal flow that we will calculate below, albeit using a different approach and in a more general form. However, Bell (1975b) does not use their equation to investigate the case with both mean and tidal flow, but instead considers the two separately.

The relevant hydrostatic equations, linearized about a uniformly stratified state, are

$$\frac{\partial \tilde{u}}{\partial t} - f\tilde{v} + \mathbf{U}_0 \cdot \nabla_h \tilde{u} = -\frac{1}{\rho_0}\frac{\partial \tilde{p}}{\partial x}, \tag{5a}$$

$$\frac{\partial \tilde{v}}{\partial t} + f\tilde{u} + \mathbf{U}_0 \cdot \nabla_h \tilde{v} = -\frac{1}{\rho_0}\frac{\partial \tilde{p}}{\partial y} \tag{5b}$$

$$0 = -\frac{1}{\rho_0}\frac{\partial \tilde{p}}{\partial z} + \tilde{b}, \tag{5c}$$

$$\frac{\partial \tilde{b}}{\partial t} + \tilde{w}N^2 + \mathbf{U}_0 \cdot \nabla_h \tilde{b} = 0, \qquad \text{and} \tag{5d}$$

$$0 = \frac{\partial \tilde{u}}{\partial x} + \frac{\partial \tilde{v}}{\partial y} + \frac{\partial \tilde{w}}{\partial z}, \tag{5e}$$

where N is the buoyancy frequency, ρ_0 the reference density, and other parameters are as defined previously. Consistent with classical theory, the advection due to the tidal flow is neglected under the assumption of a small tidal excursion distance $U_t/\omega_t \ll L$, where ω_t is the (Eulerian) tidal frequency and L the length scale of topography. Solutions to (5) are plane waves moving with the background flow,

$$\tilde{w} = \Re(\hat{w}(k, l, m, \omega) \exp\{-i[k(x - U_0 t)$$
$$+ l(y - V_0 t) + mz - \omega t]\})$$
$$= \Re\{\hat{w}(k, l, m, \Omega) \exp[-i(kx + ly + mz - \Omega t)]\}, \tag{6}$$

where $i = \sqrt{-1}$, k and l are the x and y wavenumbers, respectively, ω is the intrinsic frequency, $\mathbf{K} = (k, l, 0)$ is the net horizontal wavenumber with modulus $|\mathbf{K}| = K = \sqrt{k^2 + l^2}$, $m = \pm NK/\sqrt{\omega^2 - f^2}$ is the vertical wavenumber, and $\Omega = \omega + \mathbf{K} \cdot \mathbf{U}_0$ is the absolute (Eulerian frame) frequency. The boundary condition on the system is that flow must be parallel to the topography $h(x, y)$ or, in the small amplitude approximation,

$$\tilde{w}|_{z=0} = [\mathbf{U}_0 + U_t \cos(\omega_t t)\hat{\mathbf{x}}] \cdot \nabla h$$
$$= \Re\left\{-i\mathbf{K}\hat{h}e^{-i(kx+ly)} \cdot \left[\mathbf{U}_0 + U_t\hat{\mathbf{x}}\frac{1}{2}(e^{-i\omega_t t} + e^{i\omega_t t})\right]\right\}, \tag{7}$$

or

$$\hat{w} = \begin{cases} -i\hat{h}\,\mathbf{K} \cdot \mathbf{U}_0, & \text{for} \quad \Omega = 0, \\[2mm] -i\hat{h}\dfrac{kU_t}{2}, & \text{for} \quad \Omega = \omega_t, \\[2mm] -i\hat{h}\dfrac{kU_t}{2}, & \text{for} \quad \Omega = -\omega_t. \end{cases} \tag{8}$$

From (5) and (6), it may be shown that the horizontal velocity amplitudes are related to the vertical amplitude via

$$\hat{\mathbf{u}}_h = \pm\frac{N}{\omega K \sqrt{\omega^2 - f^2}}(-\omega k + ifl, -\omega l - ifk)\hat{w}, \tag{9}$$

and the wave buoyancy is related to the vertical velocity amplitude via

$$\hat{b} = \frac{iN^2}{\omega}\hat{w}. \tag{10}$$

The momentum flux may thus be computed as

$$\tilde{\mathbf{u}}_h \tilde{w} = \pm\left(\frac{-\mathbf{K}N}{K\sqrt{\omega^2 - f^2}}\Re\{\hat{w}\exp[-i(kx + ly - \omega t)]\}^2 \right.$$
$$+ \frac{f(-l, k)}{\omega K \sqrt{\omega^2 - f^2}}\Re\{\hat{w}\exp[-i(kx + ly - \omega t)]\}$$
$$\left. \times \Im\{\hat{w}\exp[-i(kx + ly - \omega t)]\}\right). \tag{11}$$

At this point it is useful to define the time averaging operator,

$$\langle \rangle = \frac{1}{T}\int_0^T dt, \tag{12}$$

where T is an integer number of wave periods, and take the average value of the momentum flux,
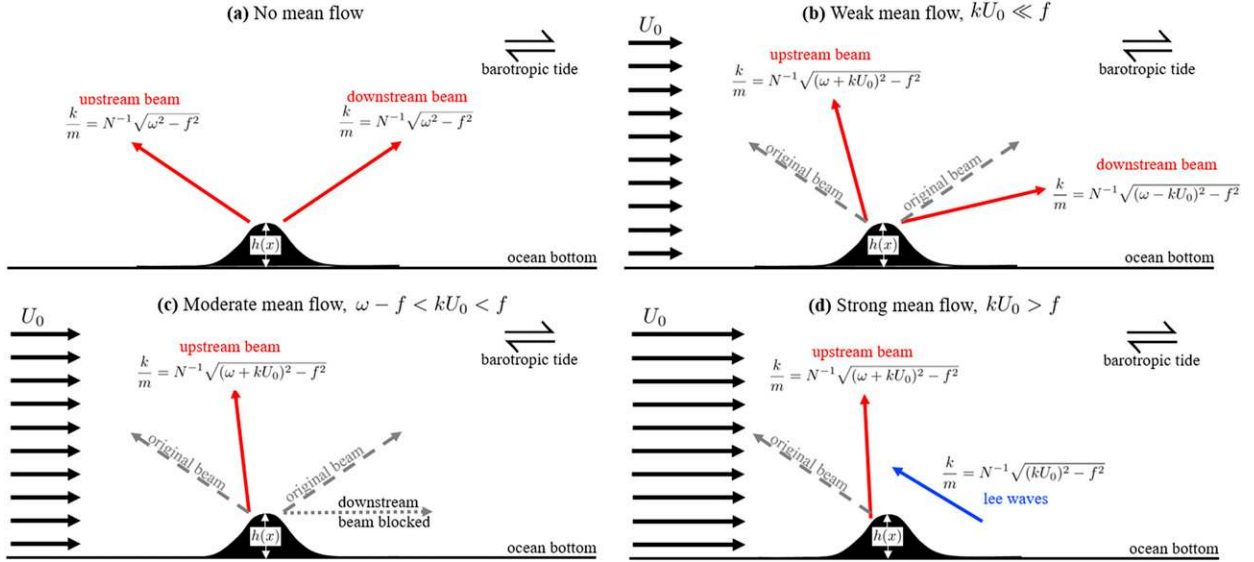
FIG. 1. The generation of waves by two-dimensional ridge topography $h(x)$ associated with a mean bottom flow U_0 of varying strength and a barotropic tide $U_t \cos\omega t$. (a) Zero mean flow with symmetric tidal generation. (b) Weak mean flow. The upstream (left) tidal beam is upshifted in Lagrangian frequency to $\omega + kU_0$. It has an increased slope k/m and larger EP flux. The opposite is true for the downstream beam. (c) Moderate mean flow where the downstream beam becomes subinertial and is blocked. The upstream beam is steeply sloped. (d) Strong mean flow resulting in lee wave generation. Upstream tidal generation is still present but typically weaker than the lee waves.

$$\langle \tilde{\mathbf{u}}_h \tilde{w} \rangle = \pm \frac{-\mathbf{K}N}{K\sqrt{\omega^2 - f^2}} \frac{|\hat{w}|^2}{2}. \qquad (13)$$

$$\langle f\hat{\mathbf{z}} \times \tilde{\mathbf{u}}\tilde{b}/N^2 \rangle = \pm \frac{\mathbf{K}f^2 N}{\omega^2 K\sqrt{\omega^2 - f^2}} \frac{|\hat{w}|^2}{2}. \qquad (14)$$

We now perform the same operations for the cross product of the buoyancy flux to obtain,

The EP flux (3) is the sum of the momentum (13) and buoyancy (14) fluxes,

$$\mathbf{F}_{\mathrm{EP}} = \pm \langle \tilde{\mathbf{u}}_h \tilde{w} + f\hat{\mathbf{z}} \times \tilde{\mathbf{u}}\tilde{b}/N^2 \rangle = \mp \frac{\mathbf{K}N\sqrt{\omega^2 - f^2}}{\omega^2 K} \frac{|\hat{w}|^2}{2} = \mp \frac{\mathbf{K}N\sqrt{\omega^2 - f^2}}{2\omega^2 K}|\hat{h}|^2 \begin{cases} |\mathbf{K} \cdot \mathbf{U}_0|^2, & \text{for} \quad \Omega = 0 \\ \dfrac{k^2 U_t^2}{4}, & \text{for} \quad \Omega = \pm\omega_t \end{cases}, \qquad (15)$$

where the minus is for vertical wavenumber $m > 0$ and the plus for $m < 0$.

Equation (15) for the wave EP flux is similar to the expression for the stress at topography due to wave generation in a combined mean and tidal flow obtained by Bell [1975b, see (3) therein]. The Bell (1975b) result is more general than our own since they do *not* make the small-excursion and hydrostatic approximations. However, the form derived here is sufficient for our purposes.

Equation (15) exhibits four different regimes, depending on the magnitude of the Doppler shift $|\mathbf{K} \cdot \mathbf{U}_0|$. Figure 1 illustrates the simplest situation of a mean and tidal flow perpendicular a two-dimensional ridge $h(x)$ giving rise to radiating beams with slope

$$\left|\frac{k}{m}\right| = \frac{\sqrt{(\Omega - kU_0)^2 - f^2}}{N},$$

for Eulerian frequency Ω (equaling ω_t for tides and 0 for lee waves). Waves propagating in the $+x$ $(-x)$ direction have $k > 0$ $(k < 0)$. More complicated three-dimensional topography will be treated below. The case of zero mean flow (Fig. 1a) is the classical limit where a symmetric topography will produce two equal and opposite tidal beams. For a weak mean flow ($kU_0 \ll f$; Fig. 1b) the two beams will be tilted consistent with advection by the mean flow (Doppler shifting), giving rise to a net momentum flux in the upstream direction (since this has the steeper beam). For moderate mean flow ($\omega - f < kU_0 < f$; Fig. 1c), the downstream beam becomes
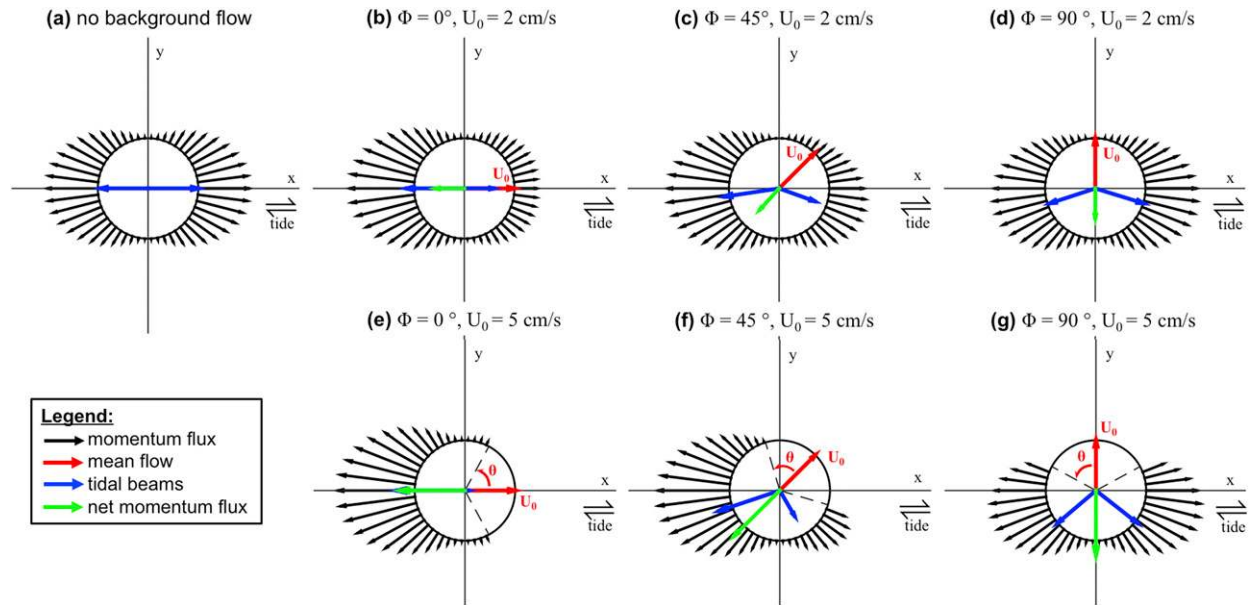
FIG. 2. (a)–(g) Internal tide generation by a zonal barotropic tide in the presence of a mean bottom flow of magnitude U_0 in the direction Φ, as indicated on each plot. Black vectors represent the magnitude of wave EP flux associated with the wave vector (k, l) in that direction assuming isotropic topography of fixed $K = \sqrt{k^2 + l^2} = 2\pi/10$ km. The fluxes are normalized with respect to the peak magnitude without a background flow where fluxes are exactly symmetric in (a). For nonzero bottom flow, internal tide generation is enhanced in the direction opposite to the mean flow, and reduced in direction of the mean flow. Generation is blocked entirely within an angle θ of the mean flow, where $\cos\theta = (\omega_t - |f|)/(U_0 K)$. The blue vectors show the tidal beams in each case, and the green vector is the net momentum flux obtained by summing the two beams.

subinertial and is blocked, leaving only a steeply sloped upstream beam. Last, for strong mean flow ($kU_0 > f$; Fig. 1d), lee waves are generated in addition to the upstream tidal beam. The lee wave momentum flux (directed upstream; scales with U_0^2) will likely be significantly larger than the tidal flux (scales with U_t^2) since in this limit we expect $U_0 \gg U_t$.

Here we focus on the cases shown in Figs. 1b and 1c where the Doppler shift is small, $|\mathbf{K} \cdot \mathbf{U}_0| < f$, for which there are no lee waves and the (tidal) EP flux is

$$\mathbf{F}_{EP} = \frac{\mathbf{K}}{4K} \frac{Nk^2 U_t^2 \sqrt{(\omega_t - \mathbf{K} \cdot \mathbf{U}_0)^2 - f^2}}{(\omega_t - \mathbf{K} \cdot \mathbf{U}_0)^2} |\hat{h}(k, l)|^2. \quad (16)$$

This result (16) is obtained by summing over the positive and negative frequencies and taking upward propagating solutions (i.e., phase velocity $\Omega/m < 0$). The EP flux defined by (16) is visualized in Fig. 2 for isotropic topography [i.e., $|\hat{h}|^2(k, l) = |\hat{h}|^2(K)$] of given wavenumber K, here assumed to be $2\pi/10$ km. The momentum flux of the internal tide in a given direction is shown as a black vector in that direction. Figure 2a displays the usual tidal generation paradigm without a mean bottom flow. The internal tide is generated in a symmetric fashion with two equal magnitude beams in

the $\pm x$ directions (indicated by blue vectors). Thus, there is zero net momentum flux in this situation. The remaining plots show the momentum fluxes for the same topography but in the presence of a background mean flow (indicated by the red vector) of strength U_0 and angle ϕ, relative to the tide. The momentum fluxes are drawn to the same scale as in Fig. 2a, enabling a direct comparison. Figure 2b displays the situation where a mean flow of $2\,\mathrm{cm\,s^{-1}}$ is aligned with the tide (in the $+x$ direction). Internal waves in the direction of the mean flow are downshifted in frequency, reducing their momentum flux. Internal waves propagating against the mean flow are upshifted in frequency, increasing their momentum flux. As a result, the downstream beam is weakened and the upstream beam strengthened, leading to a net upstream momentum flux (shown by the green vector). If the mean flow is increased to $5\,\mathrm{cm\,s^{-1}}$, as shown in Fig. 2e, these effects are amplified. The Doppler shift on downstream waves is now sufficient to make their frequency subinertial, and thus entirely block their generation. Specifically, the condition for blocking is $|\mathbf{K} \cdot \mathbf{U}_0| = KU_0 \cos\theta > \omega_t - |f|$, where θ is the angle between the wave vector and bottom flow (indicated in the figure). Thus, the blocking angle increases from 0° at small mean flow speeds to 90° at large flow speeds.

Figure 2c shows the tidal EP flux for a $2\,\mathrm{cm\,s^{-1}}$ mean flow oriented at 45° to the barotropic tide. In this situation, the tidal beams are similar in magnitude to the 0° case but with different orientation. The beams remain largely zonal but are deflected slightly opposite to the mean flow direction, resulting in their sum (the net EP flux; green vector) again being directly opposite the mean flow direction. A similar effect is seen for the mean flow oriented at 90° (Fig. 2d). As for the 0° cases, the effects are enhanced when the mean flow is increased to $5\,\mathrm{cm\,s^{-1}}$ (Figs. 2f,g). In all cases the net momentum flux is directed opposite to the mean flow.

THE NET EP FLUX

The net (space integrated) momentum flux arising from (16) is the sum over all wavenumbers, or

$$\mathbf{F}_{\mathrm{EP}}^{\mathrm{net}} = \frac{1}{4\pi^2}\int_{-\infty}^{\infty}\int_{-\infty}^{\infty}\frac{\mathbf{K}}{K}\frac{Nk^2 U_t^2\sqrt{(\omega_t - \mathbf{K}\cdot\mathbf{U}_0)^2 - f^2}}{(\omega_t - \mathbf{K}\cdot\mathbf{U}_0)^2}|\hat{h}(k,l)|^2\,dk\,dl. \tag{17}$$

We now define $\mathbf{U}_0 = U_0(\cos\phi, \sin\phi)$ and $\mathbf{K} = K(\cos\zeta, \sin\zeta)$, whereby (17) becomes

$$\mathbf{F}_{\mathrm{EP}}^{\mathrm{net}} = \frac{1}{4\pi^2}\int_0^{\infty}\int_{-\pi}^{\pi}\cos^2\zeta(\cos\zeta, \sin\zeta)$$
$$\times\frac{NK^2 U_t^2\sqrt{[\omega_t - KU_0\cos(\zeta - \phi)]^2 - f^2}}{[\omega_t - KU_0\cos(\zeta - \phi)]^2}$$
$$\times|\hat{h}(K,\zeta)|^2 K\,dK\,d\zeta. \tag{18}$$

Equation (18) implies that in the absence of a mean flow, the net EP flux is identically zero for any topography (whether isotropic or anisotropic). To obtain this result note that $|\hat{h}(k, l)| = |\hat{h}(-k, -l)|$ for any real topography, or equivalently $|\hat{h}(K, \zeta)| = |\hat{h}(K, \zeta + \pi)|$. Thus, with $U_0 = 0$, the angular integral in (18) becomes

$$\int_{-\pi}^{\pi}\cos^2\zeta(\cos\zeta, \sin\zeta)|\hat{h}(K,\zeta)|^2\,d\zeta$$
$$= \int_{-\pi}^{0}\cos^2\zeta(\cos\zeta, \sin\zeta)|\hat{h}(K,\zeta)|^2\,d\zeta + \int_0^{\pi}\cos^2\zeta(\cos\zeta, \sin\zeta)|\hat{h}(K,\zeta)|^2\,d\zeta,$$
$$= \int_{-\pi}^{0}\cos^2\zeta(\cos\zeta, \sin\zeta)|\hat{h}(K,\zeta)|^2\,d\zeta + \int_{-\pi}^{0}\cos^2(\zeta' + \pi)[\cos(\zeta' + \pi), \sin(\zeta' + \pi)]|\hat{h}(K,\zeta' + \pi)|^2\,d\zeta',$$
$$= \int_{-\pi}^{0}\cos^2\zeta(\cos\zeta, \sin\zeta)|\hat{h}(K,\zeta)|^2\,d\zeta - \int_{-\pi}^{0}\cos^2(\zeta')[\cos(\zeta'), \sin(\zeta')]|\hat{h}(K,\zeta')|^2\,d\zeta',$$
$$= (0, 0).$$

Thus, a mean flow U_0 is required for internal tide generation at any *smooth* topography to result in a net momentum flux—the result does not apply for abrupt topography of the sort considered by St. Laurent et al. (2003).

Scaling for weak bottom flow and isotropic topography

Deep ocean velocities are typically small (perhaps a few $\mathrm{cm\,s^{-1}}$), and it is thus useful to consider the limit of (18) for small flow speeds. Specifically, we will assume that $KU_0 \ll (\omega_t - |f|)$, ruling out the blocking regime discussed above (e.g., Figs. 2e–g), and take a first order expansion of (18) for small KU_0 to obtain

$$\mathbf{F}_{\mathrm{EP}}^{\mathrm{net}} \simeq \frac{1}{4\pi^2}\int_0^{\infty}\int_{-\pi}^{\pi}\cos^2\zeta(\cos\zeta, \sin\zeta)\frac{NK^3 U_t^2\sqrt{\omega_t^2 - f^2}}{\omega_t^2}\left[1 - \frac{(2f^2 - \omega_t^2)KU_0\cos(\zeta - \phi)}{\omega_t(\omega_t^2 - f^2)}\right]|\hat{h}(K,\zeta)|^2\,dK\,d\zeta. \tag{19}$$

As shown above, the non-U_0-dependent part of (19) integrates to zero and thus (19) simplifies to

$$\mathbf{F}_{EP}^{net} = \frac{-1}{4\pi^2} \int_0^\infty \int_{-\pi}^{\pi} \cos^2\zeta(\cos\zeta, \sin\zeta)\cos(\zeta - \phi)$$
$$\times \frac{NK^4 U_t^2 (2f^2 - \omega_t^2)}{\omega_t^3 \sqrt{\omega_t^2 - f^2}} |\hat{h}(K,\zeta)|^2 \, dK \, d\zeta. \qquad (20)$$

We further assume that the topography is isotropic, $|\hat{h}(K, \zeta)| = |\hat{h}(K)|$, permitting evaluation of the angular integral in (20) to obtain

$$\mathbf{F}_{EP}^{net} = -\frac{3NU_t^2(2f^2 - \omega_t^2)}{16\pi\omega_t^3\sqrt{\omega_t^2 - f^2}} \int_0^\infty K^4 |\hat{h}(K)|^2 \, dK \left(U_0, \frac{V_0}{3}\right)$$
$$= -\alpha U_t^2 \left(U_0, \frac{V_0}{3}\right), \qquad (21)$$

where

$$\alpha = \frac{3}{16\pi} \frac{N(2f^2 - \omega_t^2)}{\omega_t^3\sqrt{\omega_t^2 - f^2}} \int_0^\infty K^4 |\hat{h}|^2 \, dK. \qquad (22)$$

For weak mean flows over isotropic topography, (21) implies that the net EP flux due to tidal waves is always at an angle of $180° \pm 30°$ with respect to the mean flow. The scaling constant α in (22) can be evaluated for a given topography and stratification, and used in conjunction with (21) to predict the momentum flux as a function of tidal and mean flow velocities. If the generated internal tide dissipates locally (e.g., St. Laurent and Nash 2004) then (21) potentially provides a very simple parameterization for "tidal wave drag" in large-scale numerical models, similar to the lee wave drag implemented by Trossman et al. (2016), among others.

In the next section we use a numerical model to investigate the tidal momentum flux and validate the scaling given by (21)—in this numerical model we will see that the internal tide tends not to dissipate locally but instead radiates to the upper ocean.

3. Model results

We use the MITgcm (Marshall et al. 1997) in hydrostatic mode configured as a Southern Ocean–like 500-km-square zonally reentrant channel at 200-m horizontal resolution, with 200 vertical grid points. The basic model configuration is identical to that described previously in Shakespeare and Hogg (2018). The reader is referred to that paper for details, with only a summary provided here. The model is forced by full-depth temperature restoring sponges inside the north and south

walls of the domain that relax the temperature (density) field toward prescribed profiles. There are no surface buoyancy fluxes or wind stresses applied. The (constant) Coriolis frequency is $f = -1.26 \times 10^{-4} \, s^{-1}$, appropriate to the Southern Ocean. The topography (shown in Fig. 3e) consists of random roughness on scales of 10–100 km, in addition to an 800-m-high Gaussian seamount in the center of the domain (see section 4 for a comparison with realistic Southern Ocean topography). The overall root-mean-square (rms) topographic height is 112 m. The model is stabilized by a prescribed uniform horizontal diffusivity of $0.1 \, m^2 \, s^{-1}$ and a boundary-intensified horizontal viscosity as shown in Fig. 3d. These choices of subgrid parameterizations minimize the spurious linear dissipation of the wave field, while maintaining model stability (Shakespeare and Hogg 2017b). The only change to the model studied in Shakespeare and Hogg (2018) is the addition of a zonal barotropic tide, $\mathbf{u}_t(t) = (U_t \cos\omega_t t, 0, 0)$, added as a body force in the momentum equations. Here we assume the dominant M_2 tidal frequency, $\omega_t = 1.41 \times 10^{-4} \, s^{-1}$, and consider three tidal flow speeds: the reference case with no tide, $U_t = 0$, previously considered in Shakespeare and Hogg (2018), a weak tide case of $U_t = 3 \, cm \, s^{-1}$, and a strong tide case of $U_t = 9 \, cm \, s^{-1}$. The $3 \, cm \, s^{-1}$ tide is close to typical values in the (deep) Southern Ocean (Egbert and Erofeeva 2002; Arbic et al. 2004). Vertical profiles of the root-mean-square horizontal velocities and stratification in each simulation are shown in Figs. 3a–c. The tidal cases are spun up from the zero-tide case for 3 months prior to analysis. The tidal forcing inputs momentum to the model ocean purely through its interaction with the bottom topography—in a flat-bottomed model the (uniform) tidal flow would merely advect flow back and forth. In the presence of topography, tides will potentially affect the circulation both through the generation of mean and eddying flow local to the topography (i.e., tidal rectification; e.g., Young 1983; Chen and Beardsley 1995) and the radiation of the internal tide.

The simulations are analyzed using Lagrangian filtering to isolate the internal tide. This filtering technique identifies internal waves as any signal with a frequency moving with the flow (a Lagrangian or intrinsic frequency) exceeding the Coriolis frequency f [see Shakespeare and Hogg (2018) for a detailed description of the method]. The remainder of the flow is defined as the nonwave component which includes both mean and eddying flow. The filtering is performed on hourly time data over an integer number of tidal periods (99 h or 8.0 M_2 tidal periods) to limit biases due to the strong tidal signal and repeated
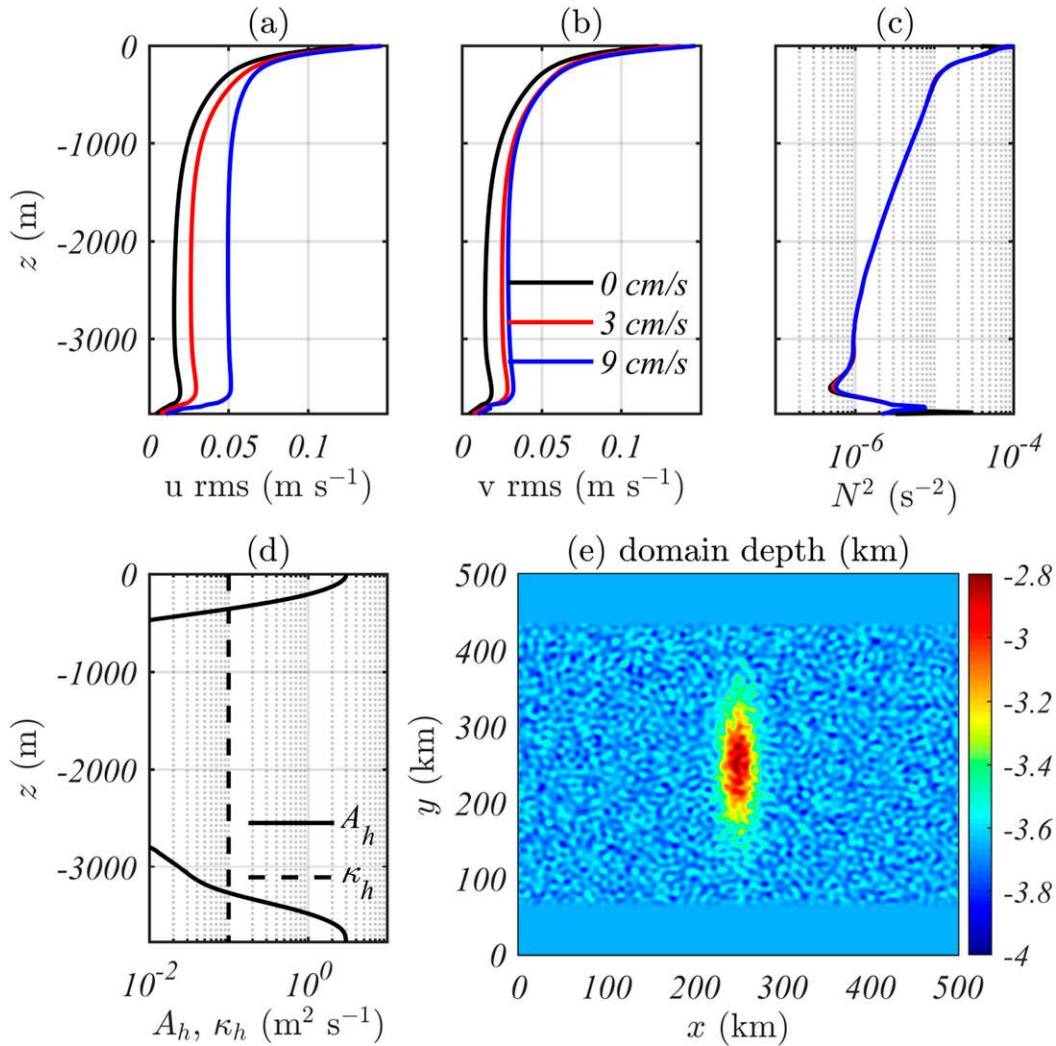
FIG. 3. Numerical model configuration. Profiles of rms time- and space-averaged velocities (a) u and (b) v for each simulation. (c) Average stratification N^2. (d) Profiles of horizontal space-averaged horizontal viscosity A_h and uniform diffusivity κ_h. (e) The depth of the zonally reentrant domain. The bottom is flat near the north and south walls where temperature-restoring sponges are applied.

for six individual 99-h periods to account for longer time-scale variability.

Figure 4 shows snapshots of the kinetic energy, strain rate, and vorticity at 10-m depth in each of the three simulations. Each plot is split into three panels showing the nonwave (left), total field (total = wave + nonwave; center), and wave (right) constituents. In each simulation the kinetic energy is dominated by an eddying current flowing eastward through the domain. Strong nonwave strain rate and vorticity is visible along this current and in the surrounding eddy field. The amplitude of the wave fields increases with larger tidal flow speeds. For the $9\,\mathrm{cm\,s^{-1}}$ tide, internal waves appear throughout the domain as background scatter in the total flow fields and are

largely uncorrelated with the more coherent nonwave flow (e.g., Fig. 4f).

a. The net internal tide momentum flux

Here we investigate the EP flux of the simulated internal tide and compare it to our theoretical predictions from section 2. The zonal and meridional components of the EP flux at 2500-m depth are displayed in Fig. 5 for the $3\,\mathrm{cm\,s^{-1}}$ (top) and $9\,\mathrm{cm\,s^{-1}}$ (bottom) simulations. The nonwave flow at 2500 m is shown by the superimposed vectors. The depth of 2500 m is chosen as it is 300 m above the highest point of the topography and thus outside the bottom boundary layer. Figure 5 illustrates that, where the nonwave flow is eastward, the zonal EP flux is predominantly westward, and where the
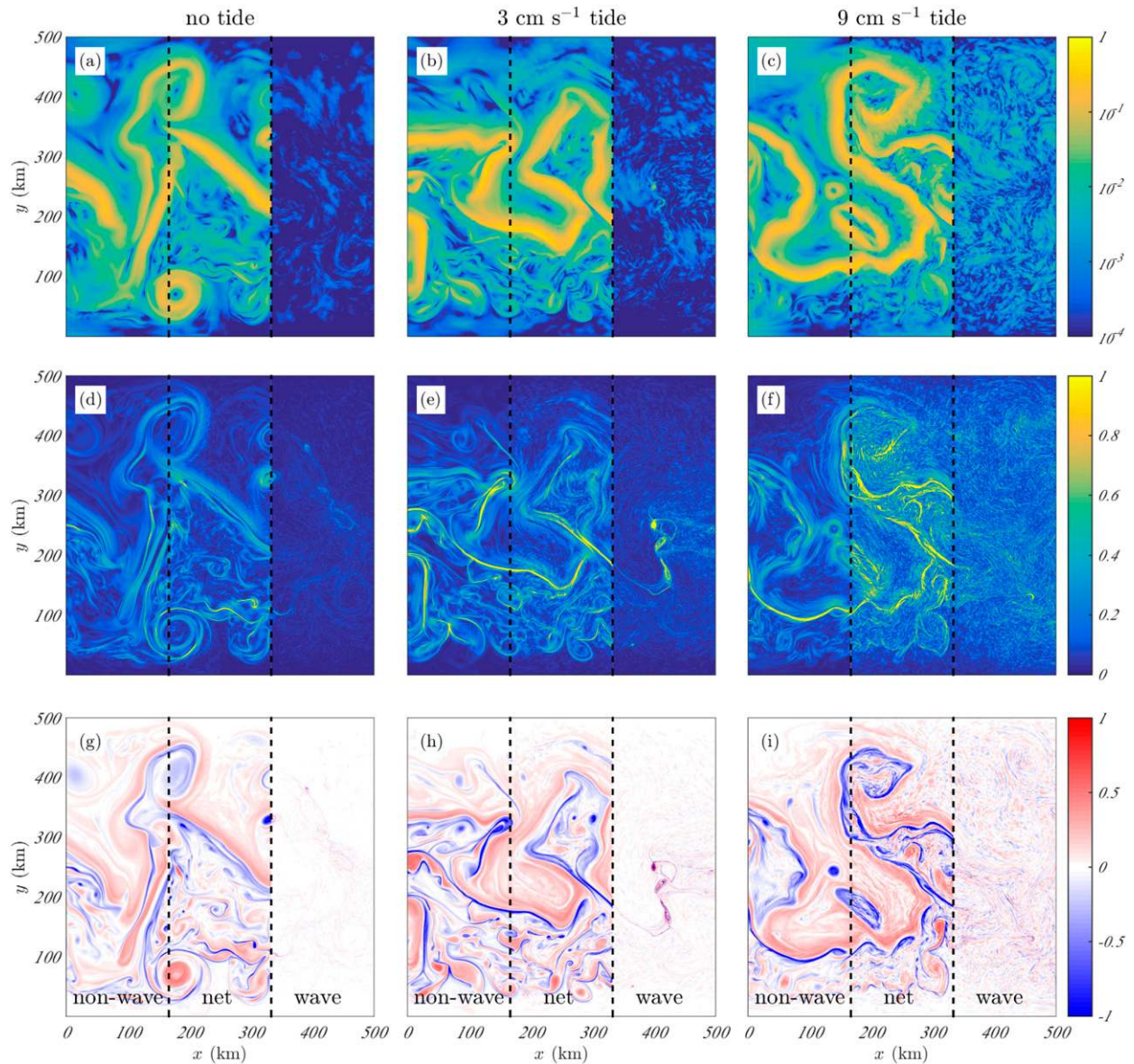
FIG. 4. Snapshots of (a)–(c) kinetic energy (m^2 s^{-2}), (d)–(f) strain rate $\sqrt{(\partial_x v + \partial_y u)^2 + (\partial_x u - \partial_y v)^2}$ normalized by $|f|$, and (g)–(i) vorticity $\partial_x v - \partial_y u$ normalized by $|f|$ from the (left) no tide; (center) 3 cm s^{-1} tide; and (right) 9 cm s^{-1} tide simulations at a depth of 10 m. In each plot, three panels are shown for each case: nonwave at left, total = wave + nonwave at center, and wave at right.

nonwave flow is predominantly northward, the EP flux is predominantly southward (and vice versa in each case). Furthermore, larger magnitude EP fluxes are observed where the nonwave flow itself is stronger. Thus, consistent with the theoretical prediction, the net EP flux is oriented against the nonwave flow and scales with the nonwave flow speed. We note that the rough bottom topography is limited to the region $60 < y < 440$ km with a flat bottom outside (see Fig. 3e), and thus no substantial wave fluxes are observed along the meridional edges of the domain in Fig. 5.

We now quantify the relationship between the nonwave flow and the EP flux, and compare with the theory. The first step is to spatially-average the time-mean EP fluxes and nonwave flow (as shown in Fig. 5) over $40\,\mathrm{km} \times 40\,\mathrm{km}$ boxes, and plot the resulting data as a histogram (Fig. 6). Only data from the region with rough topography ($60 < y < 440$ km) are included. The meridional and zonal EP fluxes are correlated against the corresponding velocity for each tidal simulation. For both components of the EP flux and both tidal flow speeds, the data shows a clear linear relationship. The lines of
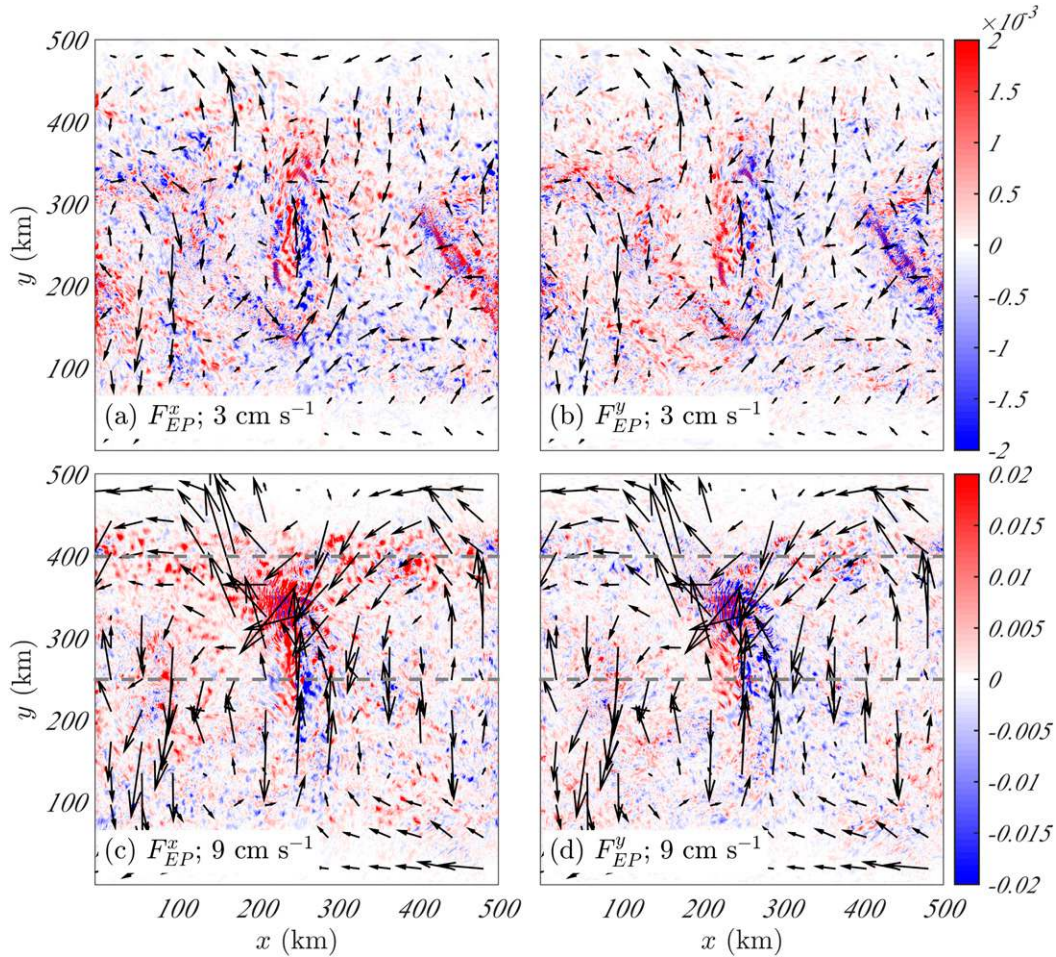
FIG. 5. The internal tide EP flux (N m^{-2}) at 2500-m depth averaged over 99 h: (a) x component for 3 cm s^{-1} tide, (b) y component for 3 cm s^{-1} tide, (c) x component for 9 cm s^{-1} tide, and (d) y component for 9 cm s^{-1} tide. Black vectors show the mean flow at each location. The EP flux generally opposes to the mean flow and is stronger for stronger mean flows, as predicted by theory. Dashed gray lines in (c) and (d) indicate the locations of transects shown in Fig. 7.

best fit are plotted in blue on Fig. 6 with correlation coefficients of 0.56–0.72. Figure 6 demonstrates that the rate of change of zonal EP flux with (nonwave) zonal velocity is larger than the rate of change of meridional EP flux with (nonwave) meridional velocity, as predicted by theory (21) (although the ratio of the best-fit slopes is less than the theoretical value of 3). The data from both EP flux components and tidal flow speeds can be amalgamated into a single plot using the theoretical scalings from (21) that $F_{EP} \equiv F_{EP}^x = 3F_{EP}^y = -\alpha U_0 U_t^2$. Figure 6c shows F_{EP}/U_t^2 plotted against flow speed, the slope of which should equal the constant α defined by (22). We compute the theoretical value of α using the mean value of N at 2500 m of 10^{-3} s^{-1} and the equivalent isotropic spectrum of the model topography to obtain $\alpha_{\text{theory}} = 0.0109$ s m^{-1}. The resulting theoretical

scaling for the EP flux is shown as a red dashed line on Fig. 6c. This value is 30% larger than the line of best fit to the data (shown in blue) which has a slope of $\alpha_{\text{fit}} = 0.0071$ s m^{-1}. A value smaller than the theory is to be expected since we are only assessing the radiating flux at 2500 m so are not capturing any momentum flux associated with waves that might dissipate below this depth, nor are we accounting for possible surface reflections.

Figure 7 displays zonal transects of the EP flux from the 9 cm s^{-1} tidal simulation. The transect locations are indicated by dashed lines on Fig. 5. The first transect (Figs. 7a,b) is taken in the center of the domain ($y = 250$ km) across the seamount. Beams are visible propagating both east and west from near the top of the seamount. Approximate two-dimensional ray paths are
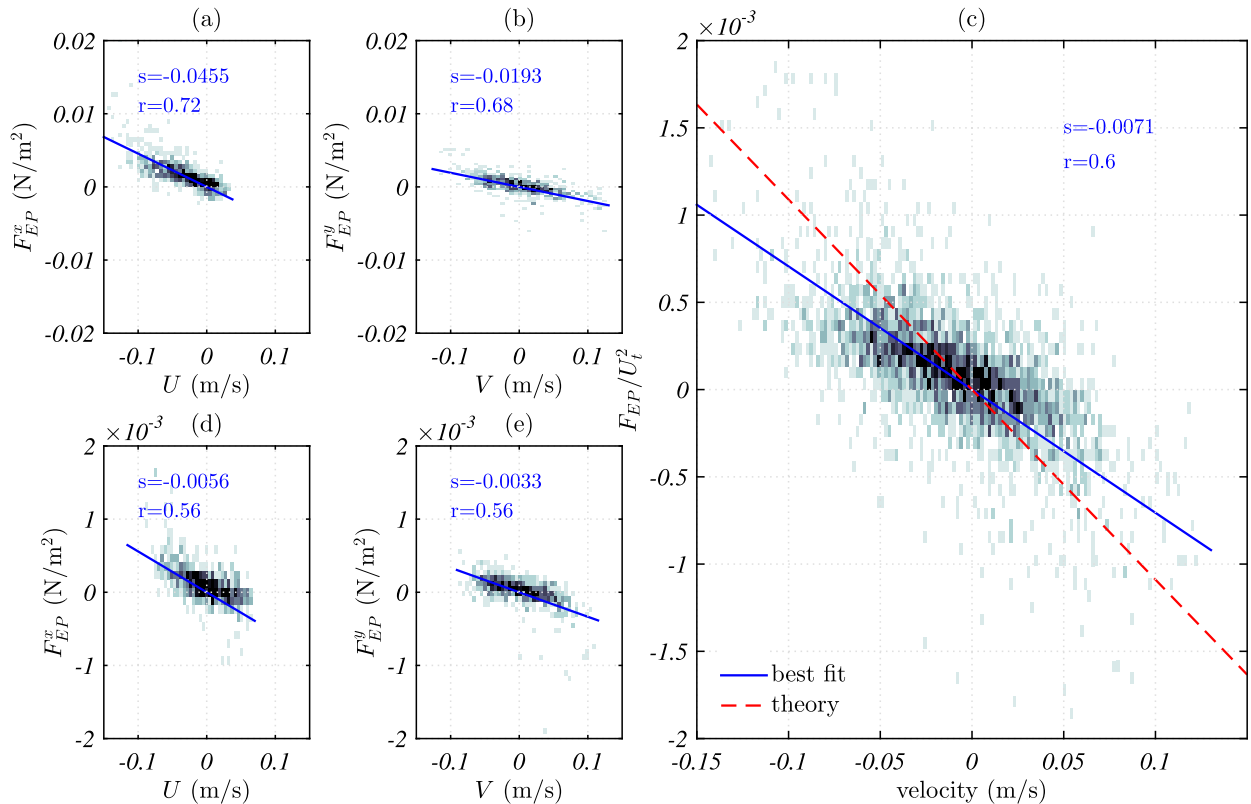
FIG. 6. Histograms of the net EP flux radiated from topography as a function of flow speed: (a) F_{EP}^x against U and (b) F_{EP}^y against V for the $9\,\mathrm{cm\,s}^{-1}$ tide; (d) F_{EP}^x against U and (e) F_{EP}^y against V for the $3\,\mathrm{cm\,s}^{-1}$ tide. The EP flux and flow velocity are computed as averages over $40\,\mathrm{km} \times 40\,\mathrm{km}$ boxes at 2500-m depth. As predicted, fluxes scale linearly with, and generally oppose, the deep mean flow. A linear fit to the data (blue) with slope s and correlation coefficient r is shown. (c) Amalgamation of all data based on the theoretical scaling; i.e., F_{EP}^x/U_t^2, $3F_{EP}^y/U_t^2$ all scale as $-\alpha U_0$ according to (21). The theoretical value of α computed from (22) is $0.0109\,\mathrm{s\,m}^{-1}$ and is shown as a red line on the plot.

displayed as black lines. These approximate paths are calculated assuming a 10-km wavelength and using only the domain-mean stratification and the time-mean zonal flow, that is, with the slope defined by

$$\frac{dz}{dx} = \frac{kN(z)}{\sqrt{[\omega_t - k\overline{u}(x,z)]^2 - f^2}}, \qquad (23)$$

in order to highlight the impact of the Doppler shift on the internal tide. The ray paths correctly identify that the eastward beam is steeper than the westward, consistent with a (small) westward component of the mean flow. The meridional EP flux associated with the eastward beam is strongly negative, owing to the strong northward mean flow on the east side of the seamount.

The second transect (Figs. 7c,d) is taken in the north of the domain ($y = 400\,\mathrm{km}$) where the mean flow is strongly westward ($>5\,\mathrm{cm\,s}^{-1}$) everywhere. Figure 7c shows that, not only is the mean EP flux eastward, but in addition, there are no clearly distinguishable westward

tidal beams. This result is unsurprising given that, according to the theory in section 2, we expect blocking of downstream tidal beams for $U_0 > (\omega_t - f)/k$, which equals $2.4\,\mathrm{cm\,s}^{-1}$ for 10-km wavelengths and $9.5\,\mathrm{cm\,s}^{-1}$ for 40-km wavelengths. Thus, the present transect is in the "blocking regime" and essentially all small-scale downstream beams should be blocked, as indicated schematically in Fig. 2e (but with the reverse mean flow direction).

The strong zonal flow at depth also leads to very steep beams, as indicated by the approximate ray paths (solid black lines) in Figs. 7c and 7d. The ray path that would result in the absence of the zonal flow [$\overline{u} = 0$ in (23)] is shown as a dashed black line. The horizontal distance traveled by the beam is only 40 km in the presence of the zonal flow, versus over 100 km without the flow. Thus, in regions of strong zonal mean flows, the wave EP flux is large and is communicated almost vertically to the ocean directly above. However, in other regions (e.g., Fig. 7a), the EP flux can be transmitted over a substantial distance horizontally, changing the spatial
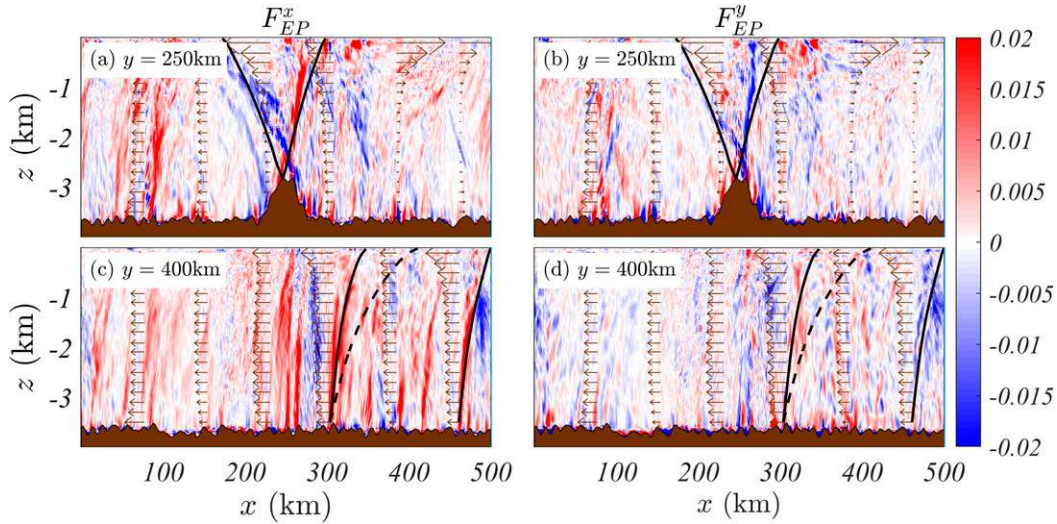
FIG. 7. Zonal transects of the (a),(c) zonal and (b),(d) meridional EP flux (N m^{-2}) in the 9 cm s^{-1} tidal simulation at (top) $y = 250$ km and (bottom) $y = 400$ km. A selection of approximate rays paths calculated from (23) are shown as black lines. The black dashed line in (c) and (d) is the ray path that would occur in the absence of the Doppler shift by the zonal flow. The zonal flow is indicated by brown arrows.

structure of the EP flux in the upper ocean relative to the deep.

While the spatial structure of the EP flux will change with height as the waves propagate, the domain-averaged value will be conserved in a slowly varying mean flow in the absence of wave dissipation (Andrews and McIntyre 1976; Bretherton 1969). The domain-averaged EP fluxes are shown in Fig. 8 for the two tidal simulations.
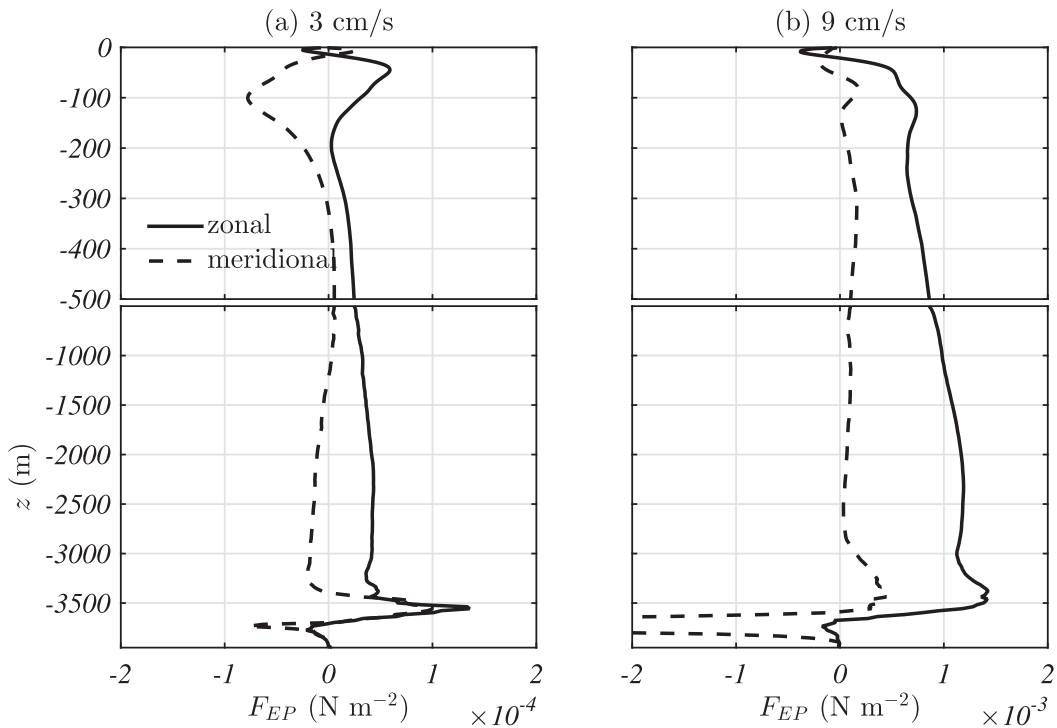

FIG. 8. The domain-averaged EP flux for the (a) 3 and (b) 9 cm s^{-1} simulations. The time average is taken over 594 h. Note that the x-axis range is an order of magnitude larger in (b) than (a).
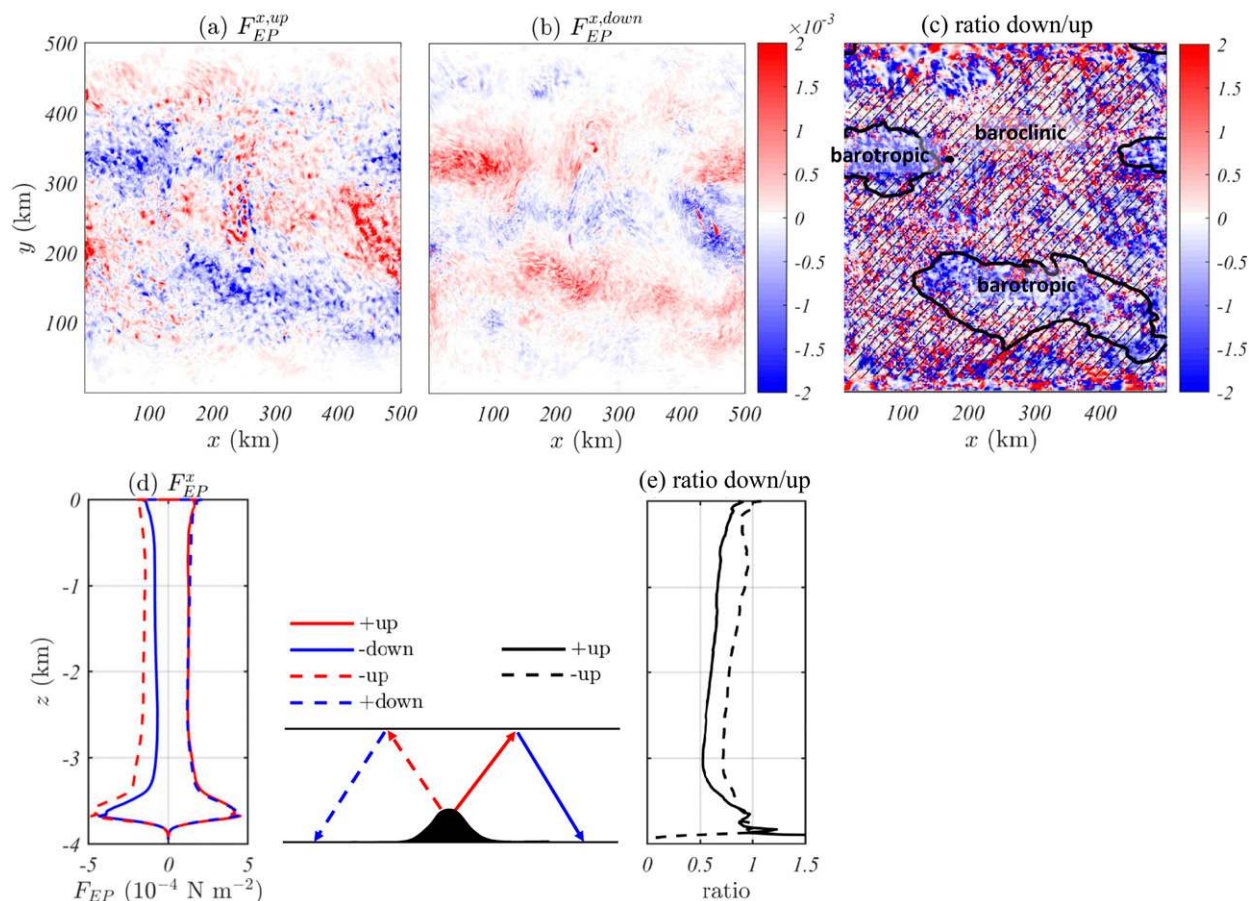
FIG. 9. Zonal EP flux $(\mathrm{N\,m^{-2}})$ for the $3\,\mathrm{cm\,s^{-1}}$ simulation, averaged over a 99-h period. EP flux associated with (a) upward and (b) downward propagating waves at 2500-m depth. (c) The ratio of upward to downward EP flux at 2500 m. Hashing indicates regions where the zonal flow—averaged over 40 km $\times$ 40 km boxes—is baroclinic (changing sign with depth). The solid black curve shows the $3\,\mathrm{cm\,s^{-1}}$ contour of zonal flow at 2500 m. (d) The domain-averaged zonal EP flux integrated separately where it is positive (eastward) and negative (westward). A surface reflection of upward positive (negative) EP flux becomes a downward negative (positive) EP flux as indicated in the schematic. (e) The ratio of downward to upward EP flux for the eastward and westward components.

The meridional EP flux (dashed line) is negligible in both simulations consistent with the small domain-averaged meridional bottom flow. The zonal EP flux (solid line) is positive in both simulations consistent with the westward bottom flow. Between the top of the topography (2800 m) and 500-m depth, the zonal EP flux decays to 74% (59%) of its original value in the $9\,\mathrm{cm\,s^{-1}}$ ($3\,\mathrm{cm\,s^{-1}}$) simulation. These losses are predominately from leakage of waves into the sponges at the meridional edges of the domain where they are dissipated. Nonetheless, the majority of the wave momentum flux is transmitted to the upper ocean (above 500 m). Here the waves interact with the strong velocity and density gradients of the near-surface region, dissipate and ultimately transfer momentum to the nonwave flow. Figure 8 shows large divergences of the EP flux in the upper ocean, especially in the top 50 m.

The upward propagating internal tide can also reflect off the surface of the model ocean. We quantify this effect by filtering the wave fields to obtain the upward and downward propagating components. This is achieved similarly to Shakespeare and Hogg (2018) by taking a Fourier transform in time and z at each (x, y), and filtering based on the sign of the vertical phase speed ω/m. The individual EP flux corresponding to the upward and downward propagating waves may then be computed and is shown in Fig. 9 for the $3\,\mathrm{cm\,s^{-1}}$ tide simulation. The upward and downward fluxes are of a similar order, indicating the presence of substantial reflections. The relative magnitude of the reflected waves (at 2500-m depth) is quantified in Fig. 9c via the ratio of the downward to upward EP flux. The ratio is close to minus 1 (implying perfect reflection) where the flow is uniformly barotropic and highly variable in regions of
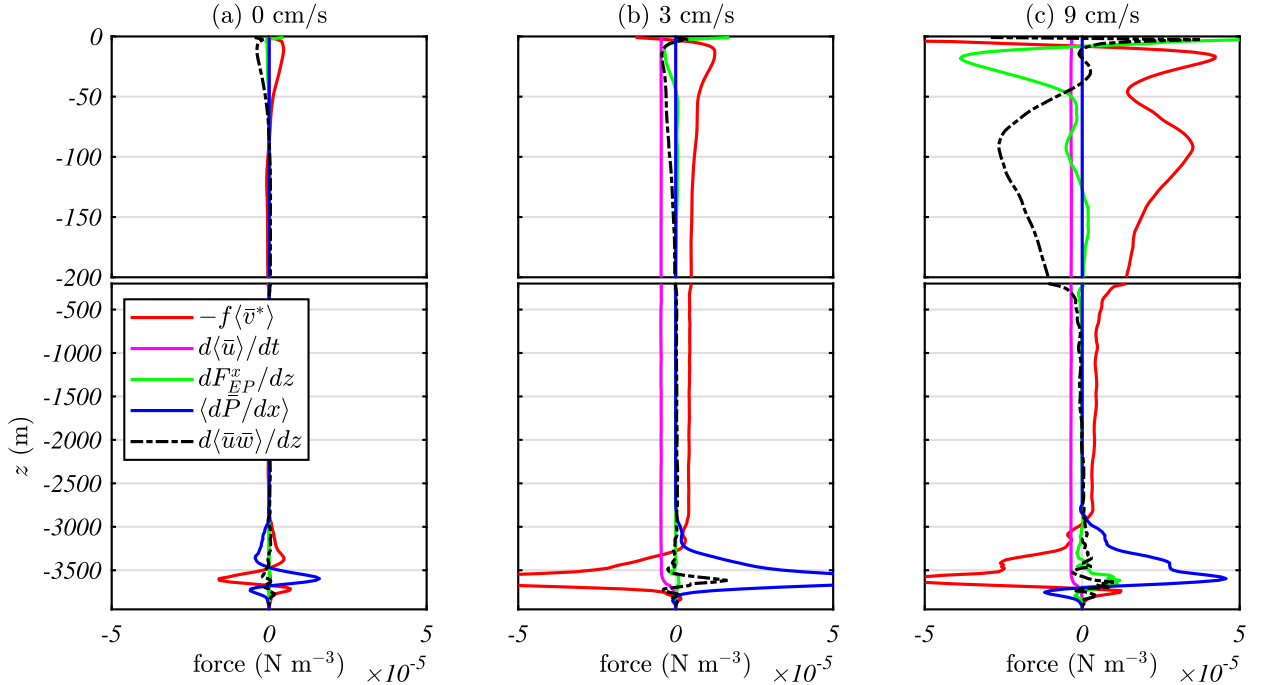
FIG. 10. The domain-averaged zonal momentum balance for the (a) 0, (b) 3, and (c) 9 cm s^{-1} simulations as per (24). The time average is taken over 594 h.

baroclinic flow (indicated by hashing). This result implies that waves are dissipating more in the upper model ocean when the flow in a given region is baroclinic, such that a wave generated in a bottom flow of a given direction, will likely end up in a near-surface flow in the opposing direction (thus permitting inertial-level dynamics; see section 4). The upward/downward wave filtering further permits identification of eastward and westward propagating waves, according to the sign of the EP flux—for example, an upward wave with a positive EP flux is going east, and if it reflects off the surface, will become a downward wave with negative EP flux (i.e., downward transport of positive zonal momentum). Thus, the ratio of the domain-averaged upward positive EP flux to the domain-averaged downward negative EP flux gives a measure of the degree of reflection of eastward propagating waves (and similarly for westward propagating). Figure 9d displays the magnitude of each of the up (down) and east (west) components of the zonal EP flux, with the ratios shown in Fig. 9e. Upward and westward waves appear to reflect about 75% of their EP flux, consistent with their generation being predominantly in regions of barotropic flow (e.g., Figs. 9a,c). By contrast, upward and eastward waves reflect about 50%, and thus the domain-averaged zonal EP flux is positive as shown previously (Fig. 8a). Analogous results apply for the 9 cm s^{-1} tide simulation (not shown).

b. Internal tides enhance upper-ocean flow

We first consider the consequences of the upper-ocean EP flux divergence for the domain-averaged zonal momentum budget. A divergence of the wave EP flux acts as a stress on the nonwave flow, as per the zonal part of (2),

$$\frac{\partial \langle \overline{u} \rangle}{\partial t} + \frac{\partial}{\partial z} \langle \overline{u}\,\overline{w} \rangle - f \langle \overline{v}^* \rangle + \left\langle \frac{\partial P}{\partial x} \right\rangle + \frac{\partial \langle F^x_{\mathrm{EP}} \rangle}{\partial z} = 0. \quad (24)$$

The pressure gradient term in (24) is associated with zonal pressure differences across bottom topography (form stress) and is zero above the height of the topography. This term is responsible for momentum transfer between the solid earth and the flow—whether wave, mean or eddying. The nonwave momentum flux divergence in (24) $\partial_z \langle \overline{u}\,\overline{w} \rangle$ is expected to be predominantly associated with eddies. However, mesoscale eddies have multimonth time scales and as such, unlike waves, are not separable from the time-mean flow in the present simulations which have only 25 days of output for analysis. Thus, only the combined nonwave flux divergence is calculated. All quantities are time averaged over a period of 25 days. In the tidal simulations there is a slow, near-barotropic evolution of the mean state over this time meaning that the time-rate-of-change term in (24) must be maintained.

Figures 10a–c display the domain-averaged zonal momentum budget in (24) for the no tide, 3 cm s^{-1}, and
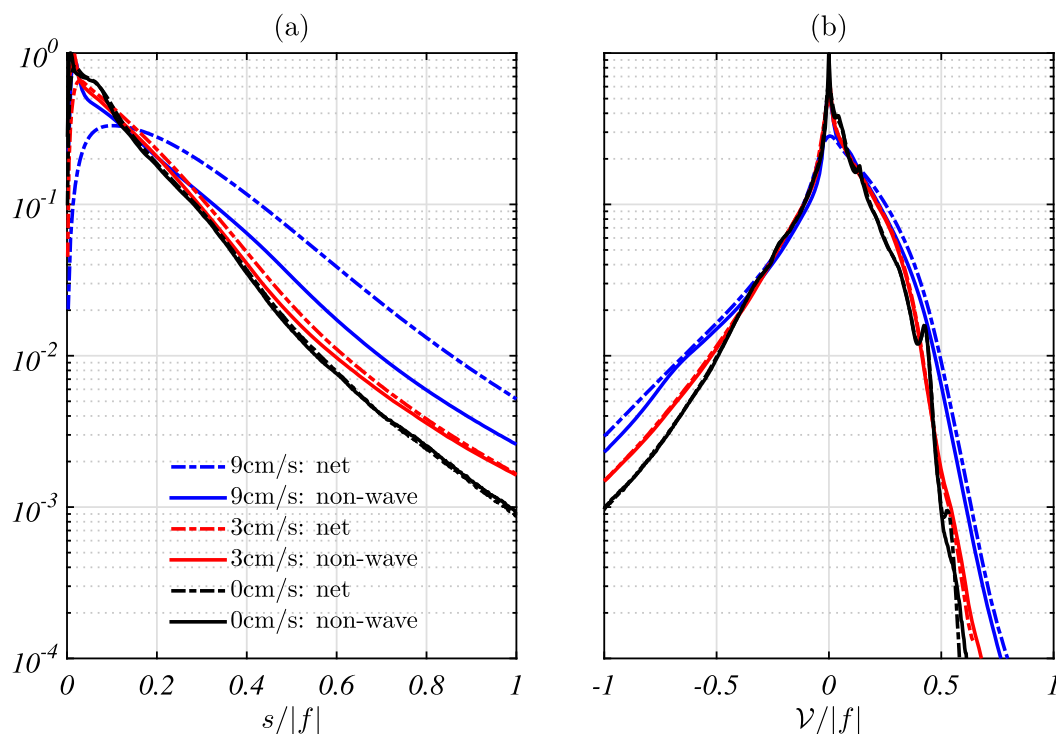
FIG. 11. Normalized probability density functions of 10-m depth flow properties of the total (wave + nonwave; dash) and nonwave only (solid) in the three simulations: (a) strain rate $s = \sqrt{(\partial_x v + \partial_y u)^2 + (\partial_x u - \partial_y v)^2}$ and (b) vorticity $\mathcal{V} = \partial_x v - \partial_y u$.

$9\,\mathrm{cm\,s^{-1}}$ tidal simulations, respectively. In the absence of a tide (Fig. 10a), the primary balance in the upper ocean is between nonwave momentum flux divergence (black dashed line; eddies) and a northward residual flow (red; Coriolis). In the deep ocean below 3000 m, the balance is between pressure differences across topography (blue) and a predominantly southward residual flow. The wave EP flux divergence (green) begins to play at role for the $3\,\mathrm{cm\,s^{-1}}$ tide (Fig. 10b), with comparable magnitude to the nonwave flux divergence in the upper 50 m. The combined nonwave and wave flux divergence is balanced by a northward residual flow. The balance in the deep ocean remains the same as in Fig. 10a, albeit with higher magnitudes. As foreshadowed above, there is a near barotropic deceleration of the zonal flow (pink) in the interior of the model ocean, balanced by a northward mean flow. For the strongest $9\,\mathrm{cm\,s^{-1}}$ tide (Fig. 10c), the near-surface balance is between the wave EP flux divergence and a strengthened northward sub-surface flow, peaking at 20-m depth. The nonwave flux divergence (eddies) is also enhanced relative to the weaker tide simulation (Fig. 10b). The interior and bottom balances in Fig. 10c remain very similar to Fig. 10b.

Figure 10 also shows that the nonwave momentum flux divergence term increases in the upper ocean with increasing tidal forcing, suggestive of a stronger eddy field. To quantify changes in near-surface eddying flow, Fig. 11 displays probability density functions (pdfs) of the strain rate and vorticity (denoted $\mathcal{V}$) at 10-m depth for each simulation, averaged over hourly snapshots (a single snapshot of these 10-m variables was shown in Fig. 4). Both the total (i.e., wave + nonwave; dash) and nonwave (solid) flow properties are displayed. The difference between the two values indicates the direct contribution of waves to the total flow strain rate and vorticity—which is small, except for the strain rate contribution for the $9\,\mathrm{cm\,s^{-1}}$ tide. However, the impact of the radiating internal tide in forcing near-surface eddying flow is indicated by the changes to the *nonwave* component with changing tidal forcing. Figure 11 shows that the distribution of nonwave (eddy) strain rate and vorticity shifts toward larger values with increasing tidal forcing—that is, eddying flow is enhanced.

We can connect changes in nonwave (eddy) vorticity[2] directly to the radiating wave momentum flux by taking

---

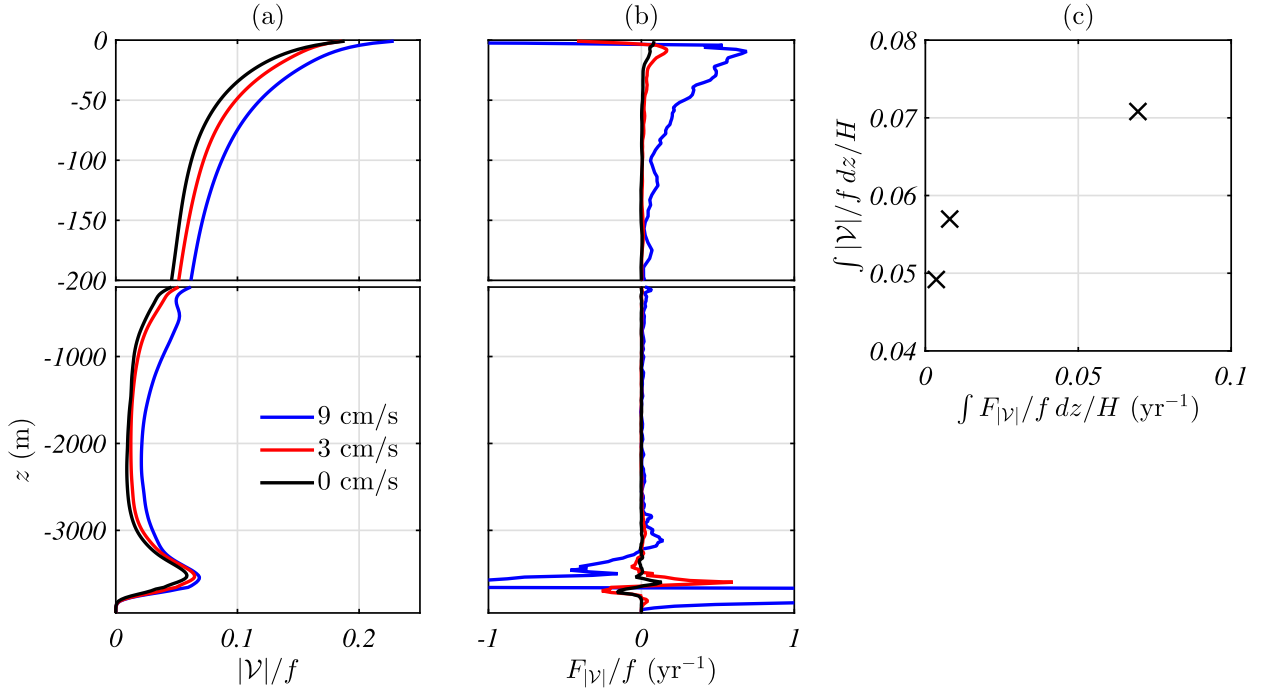[2] A similar approach can be taken for the strain rate, with comparable results.

FIG. 12. Enhancement of upper-ocean eddying flow with increased tidal forcing. (a) Time- and space-averaged nonwave vorticity modulus $|\mathcal{V}|$. (b) Time- and space-averaged wave forcing of the vorticity $F_{|\mathcal{V}|}$, as per (26). (c) Upper-ocean integrated wave vorticity $\int_{-H}^{0}|\mathcal{V}|/f\,dz/H$, where $H = 500$ m, plotted against the integrated forcing for each of the simulations.

the curl of the momentum equation (1) and horizontal space–time averaging,

$$\frac{\partial \mathcal{V}}{\partial t} = -\frac{\partial}{\partial z}\langle \nabla \times \mathbf{F}_{\mathrm{EP}}\rangle_z + \text{other non-wave contributions},$$

$$(25)$$

or in terms of the modulus of the vorticity,

$$\frac{\partial |\mathcal{V}|}{\partial t} = \underbrace{\left\langle \left[-\frac{\partial}{\partial z}(\nabla \times \mathbf{F}_{\mathrm{EP}})_z \right] \mathrm{sign}(\mathcal{V}) \right\rangle}_{\text{wave forcing: } F_{|\mathcal{V}|}}$$

$$+ \text{other non-wave contributions}. \qquad (26)$$

The "other nonwave contributions" in (25) and (26) includes large vorticity contributions from, for example, horizontal divergence of the mean flow. However, here we only compute the wave-forcing contributions to the vorticity shown explicitly in (25) and (26). Equation (26) shows that preexisting vorticity structures will be enhanced where the forcing due to waves (i.e., minus the divergence of the curl of the EP flux) has the same sign as the vorticity in that location. Given a positive wave forcing $F_{|\mathcal{V}|}$, the mean vorticity of the flow need not change, but both cyclonic and anticyclonic structures will be enhanced on average

(as seen in Fig. 11b). Figure 12 displays vertical profiles of the domain-averaged modulus of the vorticity $|\mathcal{V}|$ and the corresponding wave forcing $F_{|\mathcal{V}|}$. The vorticity increases over all depths with increasing tidal forcing, but increases most substantially in the upper ocean. The wave EP flux is acting to directly enhance the vorticity in the upper ocean, especially the upper 100 m. The magnitudes of wave forcing (i.e., $F_{|\mathcal{V}|} \sim f\,\mathrm{yr}^{-1}$) imply that the waves can turn over the upper-ocean vorticity on a time scale of months—comparable to typical eddy time scales (e.g., Imawaki 1983). Figure 12c shows the mean vorticity averaged over the upper 500 m plotted against the corresponding mean wave forcing. There is a consistent increase in the vorticity with increasing wave forcing. The mean upper-ocean vorticity increases by 15% for the 3 cm s^{-1} tide, and 44% for the 9 cm s^{-1} tide, relative to the no-tide simulation. Other eddying flow properties including strain rate and vertical shear are increased commensurately (not shown).

4. Discussion

In section 3b we showed that the upward wave momentum flux acts to directly enhance the vorticity of the upper ocean. This enhancement relies on waves preferentially dissipating and depositing momentum
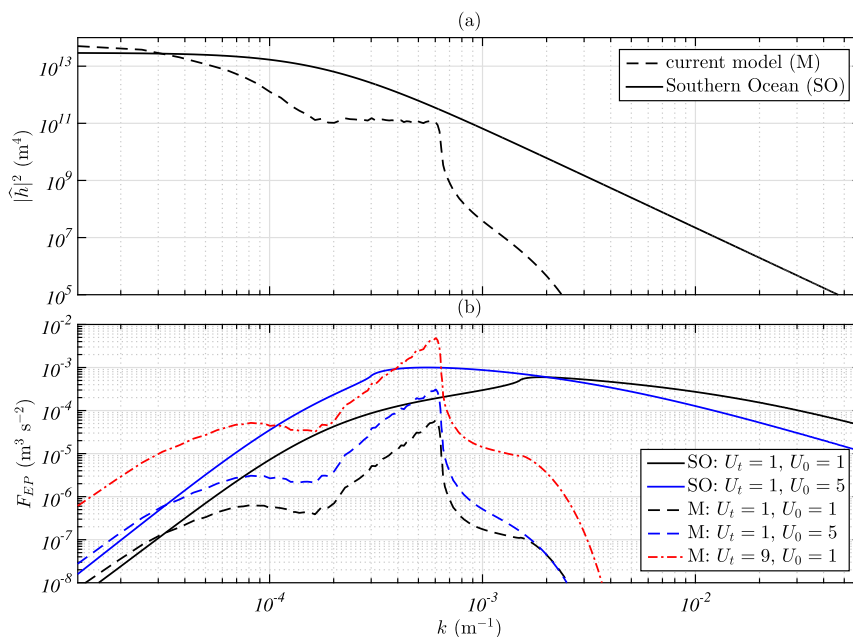
FIG. 13. Comparison of topography used in the present model with idealized topographic spectra for the Southern Ocean (Goff and Jordan 1988): the power spectra is defined by (32) of Shakespeare and Hogg (2017b) with parameter values $H_{rms} = 305$ m, $\mu = 3.5$, $k_0 = 2.3 \times 10^{-4}$ m^{-1}, $l_0 = 1.3 \times 10^{-4}$ m^{-1}, and $\phi_0 = 320°$. (a) Comparison of azimuthally averaged (equivalent isotropic) spectra. (b) Comparison of the net EP flux calculated from (16) assuming $N = 10^{-3}$ s^{-1}, a zonal mean flow U_0, and zonal tidal flow U_t as indicated in the legend (cm s^{-1}) and either the model topography (M) or Southern Ocean topography (SO) as shown in (a). The 9 cm s^{-1} tidal case shown in red has the same integrated EP flux as in the 9 cm s^{-1} simulation (10^{-3} N m^{-2}).

in an orientation aligned with the local flow. There is at least one mechanism that will lead to such a bias in wave stresses: dissipation at inertial levels (Jones 1967; Booker and Bretherton 1967; Xie and Vanneste 2017). Waves propagating up and into sheared regions such as jets or eddies in the upper ocean are downshifted in (Lagrangian) frequency when propagating with the flow, and upshifted when propagating against. The downshifting is associated with an increase in vertical wavenumber, and the upshifting a decrease. If the flow speed grows sufficiently large at some location, a wave propagating with the flow will be downshifted to the inertial frequency, at which point the vertical wavenumber approaches infinity and the wave must dissipate—this location is an inertial level. There is no equivalent process to force the dissipation of waves propagating against the flow. Thus, on average, upward propagating waves will tend to enhance preexisting flow structures by applying (on average) a stress upon dissipation in the direction of the local flow. Upper-ocean mean shears are thereby enhanced, leading to increased vorticity (as shown in Fig. 12) in addition to strain rate and vertical shear. This inertial-level mechanism is consistent with our result that

waves are more likely to dissipate in regions of baroclinic mean flow as compared with barotropic (Fig. 9).

Such enhancement by the internal tide need not depend on the presence of a net momentum flux associated with a mean bottom flow. Symmetric tidal generation with no net momentum flux will likely still produce an enhancement of the eddy field by preferential dissipation of the two equal and opposite tidal beams in mean flows oriented in the same direction as wave propagation. Indeed, enhancement of upper-ocean flow structures by internal wave momentum fluxes has previously been proposed by Muench and Kunze (2000), assuming an isotropic Garrett–Munk background wave field (Garrett and Munk 1972). Local "mean" flows may also be forced by the dissipation of a single large amplitude tidal beam (such as at the Kaena Ridge, Hawaii; e.g., Pinkel et al. 2012)

We now consider the relevance of the parameter regime explored in the present simulations to the real ocean. The dependence of the wave EP flux on flow parameters is given by (18). A key dependency in this expression is the power spectrum of the topography $|\hat{h}|^2$. Figure 13a displays the spectra of the model topography

(dashed line) consisting of an 800-m seamount (responsible for the amplitude at large scales) and random white noise topography down to a minimum 10-km scale (chosen so as to eliminate lee wave generation). The model spectra are compared with the idealized abyssal hill spectra (solid line) of Goff and Jordan (1988) with values appropriate to the Drake Passage region [as per (32) of Shakespeare and Hogg 2017b]. The rms height of the chosen Southern Ocean topography is 305 m compared with 112 m for the model topography. Figure 13b displays the net zonal EP flux as a function of wavenumber computed from (18), assuming a weak zonal tide of $1\,\mathrm{cm\,s}^{-1}$ (typical deep ocean tides are perhaps $2\,\mathrm{cm\,s}^{-1}$; e.g., Arbic et al. 2004) and zonal mean flow of either $1\,\mathrm{cm\,s}^{-1}$ (typical) or $5\,\mathrm{cm\,s}^{-1}$ (large). The larger rms height of the abyssal hill spectra and slow fall-off at high wavenumber (i.e., $k^{-3.5}$) leads to substantially larger predicted EP fluxes compared to the model topography. Increasing mean flow speed shifts the peak momentum flux from the abyssal hill spectra to larger scales—from 3.5-km wavelength at $1\,\mathrm{cm\,s}^{-1}$ to 12-km wavelength at $5\,\mathrm{cm\,s}^{-1}$. In either case, there are substantial EP fluxes at scales of tens of kilometers and smaller. The red curve in Fig. 13b shows the EP flux corresponding to the model topography and a $9\,\mathrm{cm\,s}^{-1}$ tide as studied in present simulations, with a mean flow speed of $1\,\mathrm{cm\,s}^{-1}$ chosen to replicate the average zonal EP flux of $10^{-3}\,\mathrm{N\,m}^{-2}$ (as per Fig. 8). The EP fluxes for the Southern Ocean abyssal hill spectra are an order of magnitude larger ($\sim 10^{-2}\,\mathrm{N\,m}^{-2}$ or about 10% of typical wind stresses over much of the Southern Ocean), despite using a much smaller $1\,\mathrm{cm\,s}^{-1}$ tidal amplitude.

However, there are a number of effects that will reduce the radiated flux. First, at sufficiently small scales and/or high flow speeds, the generation of upstream propagating (and upshifted) waves will also be blocked as their frequency exceeds the buoyancy frequency and nonhydrostatic effects (not considered in the present theory) become important. Thus, there will be a sharp cutoff in the EP flux at wavenumbers exceeding $k \sim N/U_0$ which equates to $k \sim 10^{-1}\,\mathrm{m}^{-1}$ for a $1\,\mathrm{cm\,s}^{-1}$ flow. Higher tidal harmonics will also be generated when $k \sim \omega_t/U_t \sim 10^{-2}\,\mathrm{m}^{-1}$ for a $1\,\mathrm{cm\,s}^{-1}$ tide. In addition, lee waves will be generated when $kU_0 > f$ and will also contribute to the momentum flux. Nonetheless, integrating the total momentum flux for the $1\,\mathrm{cm\,s}^{-1}$ tide and $1\,\mathrm{cm\,s}^{-1}$ mean flow (solid black curve) only up to lee wave cutoff ($k = f/U_0$; 500-m wavelength) yields a significant integrated flux of $0.0045\,\mathrm{N\,m}^{-2}$ for the abyssal hill topography, a factor of 4 larger than in our most extreme simulation (e.g., Fig. 8b). Thus, the parameter regime explored in our simulations, insofar as wave momentum fluxes are concerned, is well below what is present in the ocean.

As noted above, our simulations include only topographic scales exceeding 10 km, and the resulting waves predominately radiate to the upper ocean. It is likely that smaller-scale ($\sim 1\,\mathrm{km}$ or less) tidal waves would have a greater tendency to dissipate locally compared with the larger-scale waves modeled here. Thus, for realistic topography which contains a range of scales, we anticipate that larger-scale tidal waves will radiate and small-scale tidal waves may dissipate locally. Such local dissipation would act as a drag on the mean bottom flows responsible for the wave momentum flux, similar to lee wave drag (e.g., Naveira Garabato et al. 2013; Trossman et al. 2016). Therefore, tidal momentum fluxes could be important both in 1) forcing the upper ocean, as shown in the present study, and 2) acting as a drag on quasi-steady bottom flow. Further research is needed to determine what scales or wave amplitudes separate these two regimes, and how the momentum flux is partitioned between local drag and remote forcing.

5. Conclusions

In the presence of a nonnegligible mean flow, generation of the internal tide is associated with a net momentum flux directed against the mean flow. For a weak mean flow, the net momentum flux scales with the speed of the mean flow and the topographic wavenumber to the fourth power [see (21)]. For large enough mean flows, tidal generation in the direction of the bottom flow can be blocked entirely (see Fig. 2) resulting in a single upstream tidal beam. The theory was validated with a suite of wave-resolving simulations of an idealized zonally reentrant channel. The theory predicts significant momentum fluxes for typical abyssal hill topography, even for weak ($1\,\mathrm{cm\,s}^{-1}$) tidal and mean flows (Fig. 13). Thus, momentum fluxes due to the internal tide should be ubiquitous in the ocean. Previously, momentum fluxes due to internal waves have mostly been discussed in the context of lee waves (e.g., Naveira Garabato et al. 2013), which require order-of-magnitude larger velocities, and are thus less common in the deep ocean.

In our simulations, the momentum flux associated with the internal tide that radiates from the bottom topography is ultimately deposited in the upper ocean where waves interact with large near-surface flows and density gradients. This process leads to a near-surface wave-induced mean volume transport at right angles to the wave momentum flux (e.g., Fig. 10). Furthermore, the wave momentum flux acts to significantly enhance near-surface eddying flow. It is proposed that this

enhancement is a result of waves preferentially dissipating when propagating in the same direction as the local flow, consistent with inertial-level dynamics, and thereby amplifying eddying structures. The upper-ocean vorticity is increased by 44% in the simulations for the $9\,\mathrm{cm\,s^{-1}}$ barotropic tide and 15% for the $3\,\mathrm{cm\,s^{-1}}$ tide.

In summary, internal tides will both drive mean near-surface flows and enhance the strength of upper-ocean eddying flow in regions with nonnegligible bottom flows over seafloor topography. Internal tides will also provide a drag on near-bottom flows, if the waves dissipate locally. Further investigation is warranted to quantify the magnitude of this effect over the global ocean and work toward a parameterization of internal tide momentum fluxes for global ocean models.

REFERENCES

Andrews, D., and M. McIntyre, 1976: Planetary waves in horizontal and vertical shear: The generalized Eliassen–Palm relation and the mean zonal acceleration. *J. Atmos. Sci.*, **33**, 2031–2048, https://doi.org/10.1175/1520-0469(1976)033<2031:PWIHAV>2.0.CO;2.

Arbic, B. K., S. T. Garner, R. W. Hallberg, and H. L. Simmons, 2004: The accuracy of surface elevations in forward global barotropic and baroclinic tide models. *Deep-Sea Res. II*, **51**, 3069–3101, https://doi.org/10.1016/j.dsr2.2004.09.014.

Bell, T., 1975a: Lee waves in stratified flows with simple harmonic time dependence. *J. Fluid Mech.*, **67**, 705–722, https://doi.org/10.1017/S0022112075000560.

——, 1975b: Topographically generated internal waves in the open ocean. *J. Geophys. Res.*, **80**, 320–327, https://doi.org/10.1029/JC080i003p00320.

Booker, J. R., and F. P. Bretherton, 1967: The critical layer for internal gravity waves in a shear flow. *J. Fluid Mech.*, **27**, 513–539, https://doi.org/10.1017/S0022112067000515.

Bretherton, F. P., 1969: Momentum transport by gravity waves. *Quart. J. Roy. Meteor. Soc.*, **95**, 213–243, https://doi.org/10.1002/qj.49709540402.

Bühler, O., 2014: *Waves and Mean Flows.* 2nd ed. Cambridge University Press, 360 pp., https://doi.org/10.1017/CBO9781107478701.

Chen, C., and R. C. Beardsley, 1995: A numerical study of stratified tidal rectification over finite-amplitude banks. Part I: Symmetric banks. *J. Phys. Oceanogr.*, **25**, 2090–2110, https://doi.org/10.1175/1520-0485(1995)025<2090:ANSOST>2.0.CO;2.

Eden, C., and D. Olbers, 2017: A closure for internal wave–mean flow interaction. Part II: Wave drag. *J. Phys. Oceanogr.*, **47**, 1403–1412, https://doi.org/10.1175/JPO-D-16-0056.1.

Egbert, G. D., and S. Y. Erofeeva, 2002: Efficient inverse modeling of barotropic ocean tides. *J. Atmos. Oceanic Technol.*, **19**, 183–204, https://doi.org/10.1175/1520-0426(2002)019<0183:EIMOBO>2.0.CO;2.

Eliassen, A., and E. Palm, 1961: On the transfer of energy in stationary mountain waves. *Geofys. Publ.*, **22**, 1–23.

Garrett, C., and W. Munk, 1972: Space-time scales of internal waves. *Geophys. Astrophys. Fluid Dyn.*, **3**, 225–264, https://doi.org/10.1080/03091927208236082.

Goff, J. A., and T. H. Jordan, 1988: Stochastic modeling of seafloor morphology: Inversion of sea beam data for second-order statistics. *J. Geophys. Res.*, **93**, 13 589–13 608, https://doi.org/10.1029/JB093iB11p13589.

Grisouard, N., and O. Bühler, 2012: Forcing of oceanic mean flows by dissipating internal tides. *J. Fluid Mech.*, **708**, 250–278, https://doi.org/10.1017/jfm.2012.303.

Imawaki, S., 1983: Vorticity balance for mid-ocean mesoscale eddies at an abyssal depth. *Nature*, **303**, 606–607, https://doi.org/10.1038/303606a0.

Jones, W. L., 1967: Propagation of internal gravity waves in fluids with shear flow and rotation. *J. Fluid Mech.*, **30**, 439–448, https://doi.org/10.1017/S0022112067001521.

Kunze, E., 1985: Near-inertial wave propagation in geostrophic shear. *J. Phys. Oceanogr.*, **15**, 544–565, https://doi.org/10.1175/1520-0485(1985)015<0544:NIWPIG>2.0.CO;2.

——, 2017: The internal-wave-driven meridional overturning circulation. *J. Phys. Oceanogr.*, **47**, 2673–2689, https://doi.org/10.1175/JPO-D-16-0142.1.

Lamb, K. G., and M. Dunphy, 2018: Internal wave generation by tidal flow over a two-dimensional ridge: Energy flux asymmetries induced by a steady surface trapped current. *J. Fluid Mech.*, **836**, 192–221, https://doi.org/10.1017/jfm.2017.800.

Maddison, J. R., and D. P. Marshall, 2013: The Eliassen–Palm flux tensor. *J. Fluid Mech.*, **729**, 69–102, https://doi.org/10.1017/jfm.2013.259.

Marshall, J., A. Adcroft, C. Hill, L. Perelman, and C. Heisey, 1997: A finite-volume, incompressible Navier Stokes model for studies of the ocean on parallel computers. *J. Geophys. Res.*, **102**, 5753–5766, https://doi.org/10.1029/96JC02775.

McFarlane, N., 1987: The effect of orographically excited gravity wave drag on the general circulation of the lower stratosphere and troposphere. *J. Atmos. Sci.*, **44**, 1775–1800, https://doi.org/10.1175/1520-0469(1987)044<1775:TEOOEG>2.0.CO;2.

McIntyre, M., 1981: On the 'wave momentum' myth. *J. Fluid Mech.*, **106**, 331–347, https://doi.org/10.1017/S0022112081001626.

McPhaden, M., J. Proehl, and L. Rothstein, 1986: The interaction of equatorial Kelvin waves with realistically sheared zonal currents. *J. Phys. Oceanogr.*, **16**, 1499–1515, https://doi.org/10.1175/1520-0485(1986)016<1499:TIOEKW>2.0.CO;2.

Miyahara, S., Y. Yoshida, and Y. Miyoshi, 1993: Dynamic coupling between the lower and upper atmosphere by tides and gravity waves. *J. Atmos. Terr. Phys.*, **55**, 1039–1053, https://doi.org/10.1016/0021-9169(93)90096-H.

Muench, J. E., and E. Kunze, 2000: Internal wave interactions with equatorial deep jets. Part II: Acceleration of the jets. *J. Phys. Oceanogr.*, **30**, 2099–2110, https://doi.org/10.1175/1520-0485(2000)030<2099:IWIWED>2.0.CO;2.

Munk, W., 1981: Internal waves and small-scale processes. *Evolution of Physical Oceanography*, B. A. Warren and C. Wunsch, Eds., MIT Press, 264–291.

Nash, J. D., E. Kunze, J. Toole, and R. Schmitt, 2004: Internal tide reflection and turbulent mixing on the continental slope. *J. Phys. Oceanogr.*, **34**, 1117–1134, https://doi.org/10.1175/1520-0485(2004)034<1117:ITRATM>2.0.CO;2.

Naveira Garabato, A. C., A. G. Nurser, R. B. Scott, and J. A. Goff, 2013: The impact of small-scale topography on the dynamical

balance of the ocean. *J. Phys. Oceanogr.*, **43**, 647–668, https://doi.org/10.1175/JPO-D-12-056.1.

Pinkel, R., L. Rainville, and J. Klymak, 2012: Semidiurnal baroclinic wave momentum fluxes at Kaena Ridge, Hawaii. *J. Phys. Oceanogr.*, **42**, 1249–1269, https://doi.org/10.1175/JPO-D-11-0124.1.

Shakespeare, C. J., and A. McC. Hogg, 2017a: Spontaneous surface generation and interior amplification of internal waves in a regional-scale ocean model. *J. Phys. Oceanogr.*, **47**, 811–826, https://doi.org/10.1175/JPO-D-16-0188.1.

——, and ——, 2017b: The viscous lee wave problem and its implications for ocean modelling. *Ocean Modell.*, **113**, 22–29, https://doi.org/10.1016/j.ocemod.2017.03.006.

——, and ——, 2018: The life cycle of spontaneously generated internal waves. *J. Phys. Oceanogr.*, **48**, 343–359, https://doi.org/10.1175/JPO-D-17-0153.1.

St. Laurent, L., and C. Garrett, 2002: The role of internal tides in mixing the deep ocean. *J. Phys. Oceanogr.*, **32**, 2882–2899, https://doi.org/10.1175/1520-0485(2002)032<2882:TROITI>2.0.CO;2.

——, and J. D. Nash, 2004: On the fraction of internal tide energy dissipated near topography. *Near-Boundary Processes and Their Parameterization: Proc. 'Aha Huliko'a Hawaiian Winter Workshop*, Honolulu, HI, University of Hawai'i at Mānoa, 45–58.

——, S. Stringer, C. Garrett, and D. Perrault-Joncas, 2003: The generation of internal tides at abrupt topography. *Deep-Sea Res. I*, **50**, 987–1003, https://doi.org/10.1016/S0967-0637(03)00096-7.

Trossman, D. S., B. K. Arbic, J. G. Richman, S. T. Garner, S. R. Jayne, and A. J. Wallcraft, 2016: Impact of topographic internal lee wave drag on an eddying global ocean model. *Ocean Modell.*, **97**, 109–128, https://doi.org/10.1016/j.ocemod.2015.10.013.

White, R. M., 1949: The role of mountains in the angular-momentum balance of the atmosphere. *J. Meteor.*, **6**, 353–355, https://doi.org/10.1175/1520-0469(1949)006<0353:TROMIT>2.0.CO;2.

Xie, J., and J. Vanneste, 2017: Interaction between mountain waves and shear flow in an inertial layer. *J. Fluid Mech.*, **816**, 352–380, https://doi.org/10.1017/jfm.2017.39.

Young, W. R., 1983: Topographic rectification of tidal currents. *J. Phys. Oceanogr.*, **13**, 716–721, https://doi.org/10.1175/1520-0485(1983)013<0716:TROTC>2.0.CO;2.